Article

scIVNL-seq resolves in vivo single-cell RNA dynamics of immune cells during *Salmonella* infection

Zhen Xiong[1,6], Runyuan Wu[1,2,6], Yuanxin Wang[1,2,6], Yuwei Xu[1], Cunzhen Li[1,2], Deyuan Kong[3], Ziqi Xiao[1,2], Peikang Zhang[1,2], Zhonglong Wang[1,2], Peng Zhang[1], Ying Du[1], Hui Guo[1], Pingping Zhu[4], Shunmin He[1,2] ✉ & Zusen Fan[1,2,5] ✉

The immune response against pathogens involves multiple cell state transitions and complex gene expression changes. Here, we establish a single-cell in vivo new RNA labeling sequencing method (scIVNL-seq) and apply it to survey time-resolved RNA dynamics during immune response to acute enteric infection with *Salmonella*. We show that the detection of new RNA synthesis reflects more realistic information on cell activation and gene transcription than total RNA level. Interplay of RNA synthesis and degradation modulates the dynamics of total RNA. The bone marrow macrophages are first primed at a very early stage upon *Salmonella* infection. In contrast, the innate immune response of macrophages in intestine is limited. Notably, intestinal CD8^{+} T cells and plasma cells are rapidly and specifically activated at the early stage post infection. Intestinal late enterocytes quickly express MHC-I molecules and present *Salmonella* antigen to CD8^{+} T cells for their activation, serving as antigen presenting cells for the initiation of adaptive immunity. Our findings reveal the RNA control strategies and the dynamic activation rules of immune cells in response to *Salmonella* infection, challenging the doctrine boundary between innate immunity and adaptive immunity against bacterial infection.

All information that directs an organism's development and maintenance are encoded in its genomic DNA. Dynamic changes of mammalian cellular mRNA decoding from DNA are determined by the interplay of RNA synthesis, processing and degradation[1]. It is believed that cells prefer the mRNA control strategy of high RNA synthesis and degradation rate to rapidly respond to environmental stimuli, while using low RNA degradation rate to integrate transcriptional information over time[2–4]. Single-cell RNA sequencing (scRNA-seq) provides a powerful tool for disentangling RNA levels and identifying heterogeneity in cell types and states[5,6]. However, the current scRNA-seq methods only capture a snapshot of total RNA expression at the moment of measurement, ignoring the dynamic changes in RNA

transcription and degradation[2]. Genes presenting the same total RNA level can have different RNA synthesis and degradation rates, for example, where decreased transcription counteracts a slowdown in degradation. Thus, mixing of pre-existing ('old') RNAs and newly transcribed ('new') RNAs obscures the real temporal dynamics[7]. Exogenous nucleoside analogs such as 4-thiouridine (S[4]U) are commonly used for RNA metabolic labeling to distinguish new RNAs from old RNAs[8–10]. S[4]U is incorporated into new RNAs during transcription and then chemically converted to a cytidine analog. Labeled new RNAs can be distinguished from old RNAs by U-to-C conversion[11,12]. Integrating with single-cell RNA sequencing, these RNA metabolic labeling methods can simultaneously profile new and total RNA transcriptomes at

[1]State Key Laboratory of Epigenetic Regulation and Intervention, Institute of Biophysics, Chinese Academy of Sciences, Beijing, China. [2]University of Chinese Academy of Sciences, Beijing, China. [3]Nanjing Medical University, Nanjing, China. [4]School of Life Sciences, Zhengzhou University, Zhengzhou, China. [5]Faculty of Pharmaceutical Sciences, Shenzhen University of Advanced Technology, Shenzhen, China. [6]These authors contributed equally: Zhen Xiong, Runyuan Wu, Yuanxin Wang. ✉e-mail: heshunmin@ibp.ac.cn; fanz@ibp.ac.cn

single-cell resolution[2,13]. However, in vivo and time-resolved surveys of RNA dynamic changes are still absent.

Immune response to pathogenic stimuli can occur within hours and extend to a timescale of weeks, involving complex gene regulation and multiple cell state transitions[14]. The ideal immune response to pathogen infection would be primed rapidly to control the spread of pathogenic microorganisms and eliminate the potential threat, while also avoiding damage to the body itself caused by excessive and sustained immune responses[15,16]. Previous studies have utilized scRNA-seq with unprecedented resolution to quantify cell-type compositions and explore gene expression programs of immune cells under infection, especially viral infection[17,18]. However, the initial priming of immune cells and the RNA kinetics of transcription and degradation over immune responses in vivo upon infection have not been delineated. How does the interplay of RNA transcription, degradation and splicing modulate the mRNA level in a dynamic immune response? Whether genes with different functions utilize different mRNA control strategies? Do RNA transcription and degradation rates vary in different cell types under steady and stimulated conditions? These questions have not been clearly revealed, especially in an in vivo context.

Enteric *Salmonella* infection is a major public health hazard, which causes 180 million diarrheal illnesses and nearly 300 thousand deaths globally each year[19]. Beyond causing gastrointestinal symptoms such as abdominal pain and diarrhea, some serovars (for example, *S. enterica subsp. enterica serovar Typhi*) cause a systemic infection known as typhoid[20]. However, the overall survey with time-resolved dynamic changes of RNA in bone marrow (BM) and intestinal immune cells in response to *Salmonella* infection is still missing. Innate immunity serves as the first defense line against enteric pathogens, exhibiting rapid activation within hours of infection. In contrast, adaptive immune components such as T cells and B cells are considered to require a period of ~one week to be activated following pathogen exposure[14]. In this work, we establish single-cell new RNA sequencing scIVNL-seq to survey immune cell activation patterns and new RNA transcription and degradation kinetics upon *Salmonella Typhimurium* (*Salmonella*) infection. Our findings reveal in vivo RNA dynamics of immune cells during *Salmonella* infection and immune response kinetics of innate versus adaptive immunity, which challenges the doctrine boundary between innate and adaptive immunity against bacterial infection.

Results

### scIVNL-seq detects in vivo single-cell new RNA and total RNA transcriptome

To measure newly transcribed RNA in vivo, we administrated mice with S⁴U through tail vein injection to label new RNA. S⁴U integrated into new RNA was then converted into cytidine analogs, introducing T-to-C mutations during reverse transcription (Fig. 1A). Sequencing reads containing T-to-C substitutions were identified as newly transcribed RNA, and reads without T-to-C substitutions were identified as old RNA. Total RNA was the sum of newly transcribed RNA and old RNA. Given that the sequencing was based on poly-(d)T capture and priming, nascent RNAs bound on the chromatin without poly-A tails could not be detected by our current approach. As expected, S⁴U labeling caused T-to-C substitutions (Supplementary Figs. 1A and B). In addition, due to the limited S⁴U incorporation efficiency and the sequencing read length, there were some reads with the same UMI that had T-to-C substitutions, and others that had not (Supplementary Fig. 1C). In that case, the UMI was defined as labeled if there was at least one T-to-C substitution in any one of the reads linked to the same UMI index, since these reads were derived from the same transcript. New RNA presented an average of around 17% per gene and 7% per cell (Supplementary Fig. 1D). S⁴U integration and throughput expansion did not disturb the cell distribution (Supplementary Fig. 1E).

Bone marrow, as a main hematopoiesis source, is important for the immune system. We applied scIVNL-seq to detect transcriptional

activation in BM immune cells at a steady state. To visualize new RNA, we established a fluorescent labeling method based on click chemistry (Supplementary Fig. 2A). We found a significant proportion of BM cells were labeled, indicating active transcription of new RNA (Fig. 1B). To profile transcriptome of new RNA and total RNA of BM cells, S⁴U reagent was injected into mice through tail vein injection 2 h before sample collection for labeling newly transcribed RNA. Incorporation of S⁴U did not disturb total RNA profiles, and cell type clusters based on total RNA were similar to other canonical scRNA-seq data[21] (Fig. 1C). We calculated the numbers of new RNA UMIs as well as the new-to-total RNA ratios (NTRs) to reflect the extent of transcriptional activation in different cells. In fact, numbers of new RNA UMIs showed similar patterns with NTRs (Fig. 1C). Of note, new RNA transcription in hematopoietic stem cells and progenitors (HSPCs) was highly activated compared to that in differentiated cells (Fig. 1C, D). In addition, immature cell subsets, such as Ki67+ monocytes, Ki67+ neutrophils and pre-B cells possessed higher new RNA proportion than mature Ki67− monocytes, Ki67− neutrophils and mature B cells (Supplementary Fig. 2B). The numbers of genes that actively transcribing new RNA were also decreased along with cell differentiation (Supplementary Fig. 2C). These data suggest that stem progenitor cells harbor open and accessible chromatin compared to differentiated cells, and the gene expressions are gradually closed over cell differentiation, which is consistent with previous findings[22].

We next defined signature genes with new and total RNA for each cell type. Some genes vital to certain cell types were highlighted, and these genes were actively transcribed in the indicated cell types (Fig. 1E). For example, Myb regulates hematopoietic stem cell (HSC) proliferation and differentiation. Myb knockout causes a loss of self-renewal in HSCs. Klf4 is a critical regulator of monocyte and macrophage differentiation, and Gata2 is important for basophils[23]. We also noticed that some signature genes displayed low expression of new RNA, while total RNA levels were relatively high (e.g., *S100a8* and *Camp*) (Fig. 1E). Then we compared the expression of new RNA and total RNA levels of genes in each cell type. We computed pseudo-bulk levels of genes and calculated Spearman's rank correlations between labeled and total transcript levels across cell types (Supplementary Fig. 2D). *Ptprc* encoding CD45 is widely expressed in immune cells, and we found that new RNA expression pattern of *Ptprc* in different cell types was consistent with total RNA (Fig. 1F and Supplementary Fig. 2D). Both new RNA and total RNA of *Ccr2* were highly expressed in monocytes and macrophages, indicating that *Ccr2* gene harbors active transcription for maintaining high levels of total RNA in these two cell types. By contrast, some genes, such as antimicrobial peptide gene (*Camp*) and ribosomal protein L13 gene (*Rpl13*), had high levels of total RNA, whereas their new RNA was low (Fig. 1F and Supplementary Fig. 2D).

We then calculated the transcription rate (α) and half-life of mRNA ($t_{1/2}$) for these genes. We observed that *Ccr2* displayed a high rate of transcription as well as a short mRNA half-life. In contrast, *S100a9*, *Camp*, *Rpl13* and *Rpl29* were opposite to *Ccr2*, indicating low RNA turnover rates (Fig. 1G). We next wanted to determine whether new RNA expression patterns were sufficient to cluster cell types. Although post-transcriptional regulation could also modulate mRNA levels, unsupervised graph clustering with newly transcribed RNA was able to separate cell types into respective groups, which were similar to the clusters generated from total RNA. These data indicated that the synthesis of new RNA could reflect differences and characteristics of cell types (Fig. 1H and Supplementary Fig. 2E). Of note, T cells and NK cells showed highly similar new RNA transcription patterns. We noticed that basic life processes such as mRNA processing and cell cycling occupied most transcription resources in HSPCs (Supplementary Fig. 2F). Monocytes and macrophages highly expressed cytokine-mediated signaling genes. Neutrophils highly expressed respiratory burst genes, and B cells actively transcribed B cell receptor (BCR) signaling and immunoglobulin production related genes.
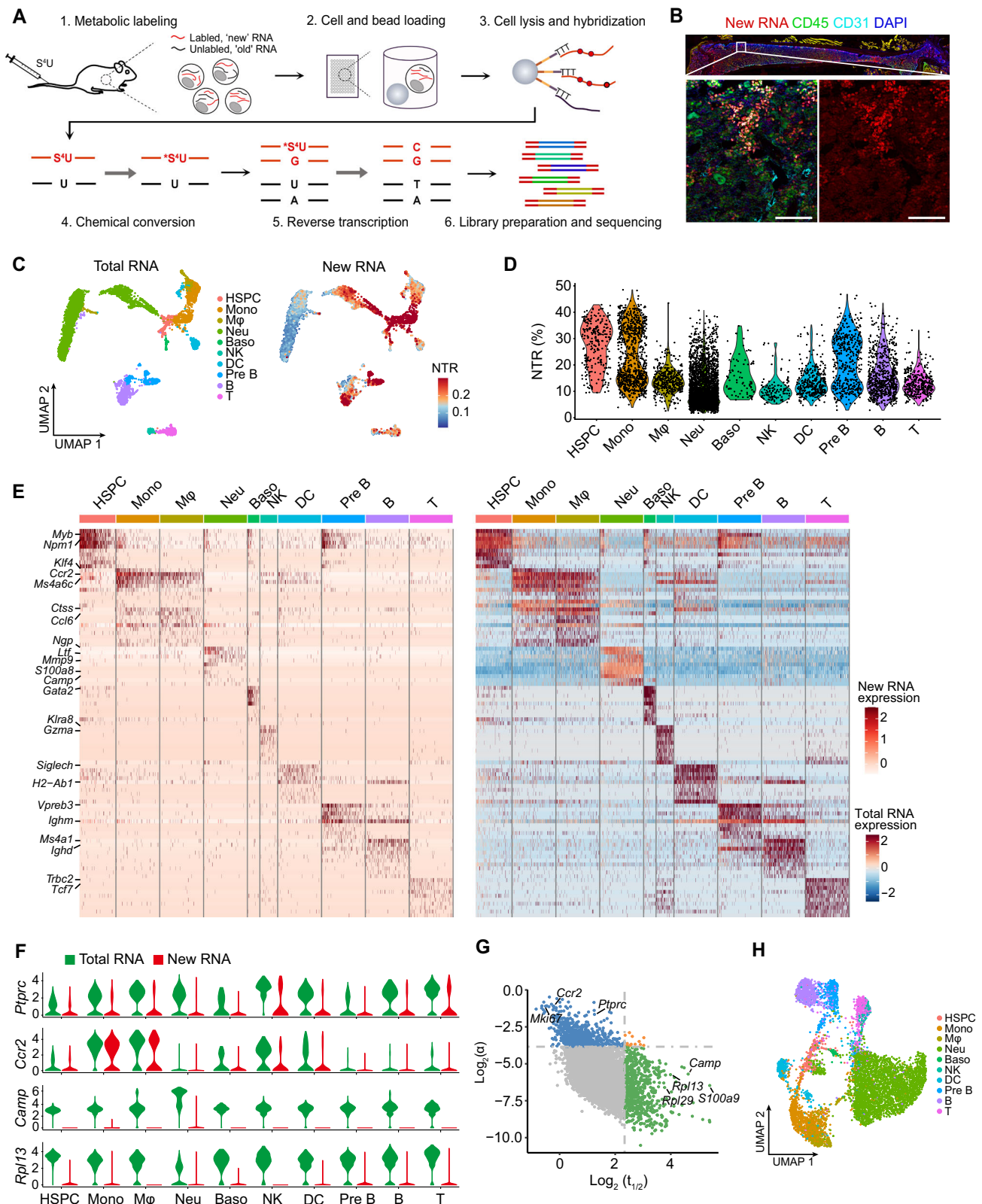
Collectively, these data confirm that scIVNL-seq is able to measure in vivo new RNA and total RNA transcriptome characters of cells.

New RNA transcription changes in response to *Salmonella* infection

Gene expression regulation is elaborately modulated during immune response, breach of which can cause pathological phenomena.

Although several reports have described transcriptomes of immune cells in response to pathogen infection[24–26], the RNA dynamics and initial priming regulation of immune cells were still unclear. Thus, we applied scIVNL-seq to detect RNA dynamics of immune cells upon *Salmonella* infection. Specific pathogen-free (SPF) mice were never infected with *Salmonella* (Supplementary Fig. 3A). To evaluate *Salmonella* invasion, we infected mice with mcherry-expressing

Fig. 1 | scIVNL-seq detects single-cell new RNA in vivo. A Overview of scIVNL-seq. S⁴U was injected into mice via tail vein injection. BM cells were collected and re-suspended. Single-cell suspensions were loaded onto microfluidic device, followed by cell lysis and mRNA capture. S⁴U integrated in new RNA was converted into cytidine analogs and was further recognized as cytosine by reverse transcriptase. cDNAs were amplified and libraries were sequenced. New RNA was identified by T-to-C substitutions. The schematic diagrams were created with Adobe Photoshop (Version 22.0.0) (**B**) New RNA (red) imaging of femur sections, co-stained with CD45 (green), CD31 (cyan) antibodies and DAPI (blue). Scale bar, 100 μm. **C** UMAP showing cell type clusters (left), UMI counts of new RNA and NTRs (right) in bone marrow CD45⁺ immune cells. The uniform manifold approximation and projection (UMAP) method was used for dimension reduction. Unique molecular identifier (UMI) counts per cell are shown as ln(count+1). Ratios of new RNA to total RNA are shown as NTRs. HSPC, hematopoietic stem and progenitor cell; Mono, monocyte; Mφ, macrophage; Neu, neutrophil; Baso, basophil; NK, natural killer cell; DC, dendritic cell; Pre B, Pre-B cell; B, B cell; T, T cell. **D** Violin plot of NTR for each BM cell type. **E** Signature gene expression of new RNA (left) and total RNA (right) for each cell type. Genes in the heatmap were the same between new RNA and total RNA. Expressions were log-normalized. **F** Total RNA and new RNA expression (log-normalized) of *Ptprc*, *Ccr2*, *Camp* and *Rpl13*. **G** Scatter plot of transcription rate (α, normalized RNA counts per cells/h) and RNA half-life (t_{1/2}, h) of genes expressed in BM cells. **H** UMAP projection of BM cell types with new RNA. Cells with new RNA data were clustered by unsupervised classification. Cell types identified with total RNA data were mapped back on UMAP projection. Source data are provided as a Source Data file.

Salmonella by oral gavage. We found that many *Salmonella* attached on intestinal villus epithelial cells at 2 h post infection, and then *Salmonella* invaded into the intestinal lamina propria at 6 h post infection (Supplementary Fig. 3B). *Salmonella* further disseminated from the gut to systemic sites. We measured bacterial load in the ileum, liver and spleen at different time points, and found remarkable increase of bacterial load after infection (Supplementary Fig. 3C). In addition, *Salmonella* infection caused rapid morbidity and mortality in mice, with dramatic body weight loss and death of mice (Supplementary Fig. 3D and E).

Then we treated *Salmonella* infected mice with S⁴U through tail vein injection 2 h before sample collections at different time points post infection (0, 2, 6, 12, 24, 48 and 72 h), and performed scIVNL-seq (Supplementary Fig. 3F). We observed that numbers of new RNA UMIs were similar between 0 and 2 h post infection and few genes changed expression significantly, suggesting no obvious response at such an early phase (Supplementary Fig. 3G and H). From 6 h to the later time points, NTR patterns were obviously changed (Fig. 2A). We found that innate immune cells such as macrophages, neutrophils and DCs enhanced the NTR early after infection (6 and 12 h), and then in later phase (24, 48 and 72 h), NTRs gradually declined (Fig. 2A), indicating a burst of new RNA transcription at early phase post infection followed by attenuation of transcription at later phase. New RNA dynamic changes of BM macrophages during *Salmonella* infection were further validated using the new RNA fluorescence imaging method (Fig. 2B). To verify the changes of NTR, we conducted biological replicates independently (batch 2) for the four key time points (0, 12, 24, and 72 h post *Salmonella* infection). Cell type clusters between the two batches were similar (Supplementary Fig. 4A). While the distribution patterns of NTR were comparable, we found that some subpopulations such as B cells and T/NK cells did show differences (Supplementary Fig. 4B). This divergence might be attributable to the heightened sensitivity of scIVNL-seq, capturing in vivo new RNA atop total RNA quantification, combined with inherent biological variability in murine responses. We then compared the changes in NTR of various cell types from the two batches at different time points after infection (Supplementary Fig. 4C). In batch 2, the NTRs of innate immune cells such as macrophages, monocytes and neutrophils were upregulated after infection, indicating the increased proportion of newly transcribed RNA, and then NTR were decreased. These trends of change after infection was consistent in the two batches (Supplementary Fig. 4C). However, there were some differences: batch 1 displayed a sharp peak of NTR at 6 h post infection followed with a dramatic decline, whereas batch 2 seemed to exhibit gentler and delayed kinetics, NTR upregulating at 12 h with much slower decline (Supplementary Fig. 4C). In addition, NTRs in stem and progenitor cells (HSPCs, Ki67⁺ monocytes and Ki67⁺ neutrophils) in batch 1 were decreased at early phase and then seemed to be recovered to some extent (Fig. 2A and Supplementary Fig. 4D). However, this variation of NTRs was different in batch 2, in which NTRs were increased at 12 and 24 h after infection (Supplementary Fig. 4D).

Total RNA describes current transcription state, while new RNA provides the vector to predict the future expression state of single cells on short timescales[27]. To describe the transcription state transition trajectory of immune cells in response to infection, we combined the total RNA and new RNA data by using *Dynamo* framework[28]. Velocity flows deduced by new RNA accurately recapitulated transcription variation of macrophages and monocytes, moving from the uninfected state (0 h) to the early activation phase (12 h) (Fig. 2C). However, cells at later infection time points (24, 48 and 72 h) were mixed with non-response state (0 h), reiterating the presence of an early phase transcriptional burst followed with deceleration to restore the transcription rate to the steady state in later phases.

We next profiled the expression of genes with upregulated new RNA transcription after *Salmonella* infection in the BM immune cells. We observed that new RNA transcription of macrophages and monocytes was dramatically evoked at 6 and 12 h (Fig. 2D). Genes related with NF-κB signaling (*Nfkbia* and *Tlr2*), pro-inflammatory cytokines (*Tnf* and *Il1b*) and chemokines (*Ccl3* and *Cxcl10*), and antibacterial substances (Serum amyloid A 3, *Saa3*) were actively transcribed at 6 and 12 h, followed by down regulation at later phases. Neutrophils and DCs actively transcribed some chemokine receptors (*Cxcr2* and *Ccr9*) at 6 h and 12 h. At later phases (24, 48 and 72 h), monocytes expressed proliferation genes (*Mki67*, *Ccnb2* and *Ccnd3*). Macrophages, monocytes and DCs upregulated expression of genes involved in antigen processing and presentation (*Tap1*, *Tapbp* and *B2m*). Notably, B cells highly expressed some neutrophil signature markers at 72 h, such as granule genes (*Camp*, *Ngp* and *Ltf*) and phagosome and endosome genes (*Rac2*, *Cybb* and *Ncf1*), suggesting some undiscovered innate-like functions of B cells in response to bacterial infection (Fig. 2D). We made a heatmap of batch 2 data with the same gene set, and the results showed a consistent expression pattern between the two batches (Fig. 2D and Supplementary Fig. 4E). However, in line with NTR variations, the new RNA expression heatmap also showed a delayed kinetics in batch 2. Transcription peaking at 12 and 24 h in batch 2 were similar with 6 and 12 h in batch 1 (Fig. 2D and Supplementary Fig. 4E). Specifically, we analyzed the total and new RNA expressions of some typical bacterial infection responding genes (*Il1b*, *Tnf*, *Tlr2* and *Saa3*). The results showed similar expression variation trends but lower level of transcriptional activity (*Il1b* and *Tnf*, at 12 h) and delayed post-activation inhibition (*Tlr2* and *Saa3*, at 24 h), indicating a weaker immune response in batch 2 (Supplementary Fig. 4F). We propose that these differences between the two batches might stem from different infection severity of mice between the two batches. Although we treated mice with the same CFU, bacteria were stored in −80 °C, some bacteria could gradually lose their viability and infection activity, leading to the attenuated actual infectious burden in batch 2, thereby dampening host immune activation and delaying transcriptional regulation. The inconsistency of NTR in stem and progenitor cells between the two batches (Supplementary Fig. 4D) might also be linked to the differences in the infection severity. Bacterial infection can mobilize HSPC proliferation, while excessive inflammation can
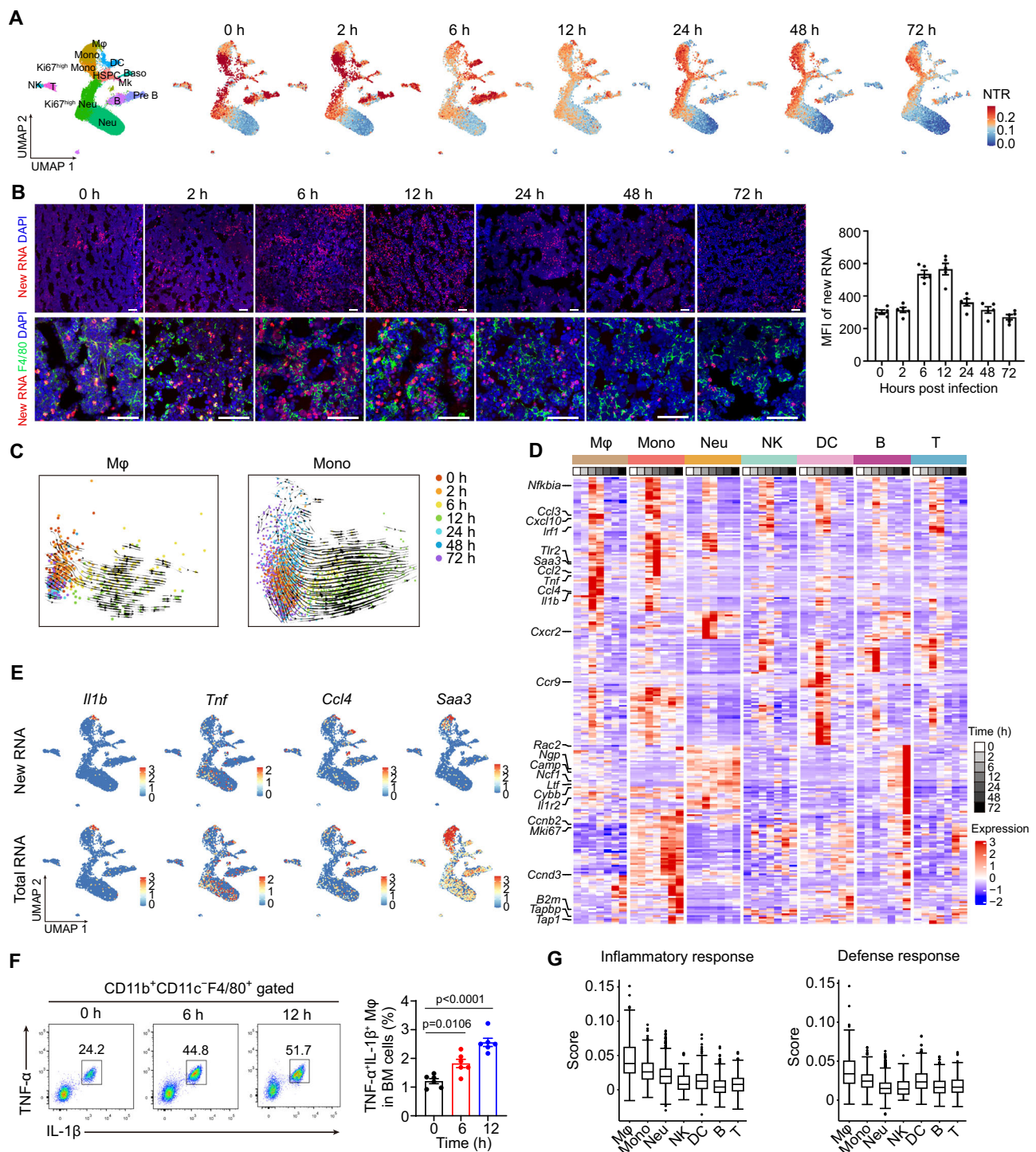
Fig. 2 | New RNA is rapidly transcribed in BM macrophages post *Salmonella* infection. A UMAP plot of CD45+ immune cells in BM and NTR at each time point post *Salmonella* infection. All cells from the indicated time points were combined to identify cell types (left). Ratio of new RNA to total RNA (NTR) was mapped onto UMAP plots (right). **B** New RNA imaging of femur sections (left) and mean fluorescence intensities (MFIs) of 5-EU labeled new RNA (right). New RNA was labeled with EU (red). Macrophages were stained with anti-F4/80 (green) antibody. Nuclei were counterstained with DAPI (blue). Scale bar, 50 μm. *n* = 5 biologically independent replicates. **C** RNA velocity flow projected in PCA space. Macrophages (left) or monocytes (right) from different time points were combined. Dynamo was used to quantify time-resolved RNA velocity. Cells are color-coded by time points. Streamlines represent integration paths connecting local projections from observed state to inferred future state. **D** Heatmap showing new RNA expression of genes with significantly up-regulated new RNA (fold change > 1.5; FDR < 0.05) in

the main BM cell types. Expression levels were scaled. *Mφ* macrophage; *Mono* monocyte; *Neu* neutrophil; *NK* natural killer cell; *DC* dendritic cell; *B* B cell; *T* T cell. **E** New RNA and total RNA expression (log-normalized) of indicated genes from sample at 6 h after infection. **F** Flow cytometry showing IL-1β and TNF-α expression of BM macrophages (CD11b+CD11c−F4/80+) at indicated post-infection time points. Proportions of IL-1β+TNF-α+ macrophages to BM cells are shown (left). *n* = 6 biologically independent replicates. Results are shown as mean ± SEM. *p* values were determined by one-way ANOVA. **G** Functional scores (inflammatory response and defense response) of new RNA for each cell type at 6 h post infection. In the box plot, the lower and upper hinges are defined as the first and third quartiles. The center represents the median, and the whiskers extend from the hinges to the largest or smallest values within 1.5× the interquartile range. Data in (**B**) and (**F**) are representative of at least three independent experiments. Source data are provided as a Source Data file.

simultaneously induce programmed cell death in these cells. The opposing effects, potentially varying with infection intensity, might be presented as differences in the NTR patterns (Supplementary Fig. 4D).

Pro-inflammatory signaling is one of the most important signaling for eliciting the immune system to eliminate detrimental stimuli in the early phase of infection. We found *Il1b* and *Tnf*, two essential mediators of inflammatory response, were most highly expressed in macrophages, both in new RNA and total RNA at 6 h (Fig. 2E). Chemokine *Ccl4* was highly expressed in macrophages and DCs. *Saa3* exerting direct antibacterial activity was mainly expressed in macrophages and monocytes (Fig. 2E). Real-time qPCR and flow cytometry data verified that IL-1β and TNF-α in macrophages were remarkably increased at 6 and 12 h post *Salmonella* infection (Fig. 2F and Supplementary Fig. 5A and B). ELISA showed the quick increase of IL-1β and TNF-α cytokines in serum (Supplementary Fig. 5C). We further quantified the extent of gene expression upregulation by calculating average fold changes of upregulated genes in different cell types. Macrophages showed the highest gene upregulation at 6 and 12 h (Supplementary Fig. 5D). Moreover, GO pathway analysis showed that macrophages were the most activated cells that expressed inflammatory and defense response genes in early infection (Fig. 2G). Taken together, BM macrophages as innate immune cells are initially activated early upon *Salmonella* infection.

scIVNL-seq reveals distinct mRNA metabolic control strategies of different genes in response to infection

Since mRNA levels are determined by the interplay of RNA synthesis, processing, and degradation, we investigated whether the change of total RNA was in accordance with new RNA variation during the immune response to infection. In macrophages, we found that new RNA was mainly upregulated at 6 h and 12 h post infection, and then numbers of upregulated new RNA were reduced over time (Fig. 3A and Supplementary Fig. 6A). Meanwhile, the number of upregulated total RNA reached a minor peak at 6 h and 12 h, and then dramatically increased at 72 h (Fig. 3A). These data suggest that in the early phase, new RNA transcription was enhanced, contributing to the rise in total RNA levels. However, in later phases, the gradually declined transcription made only a minor contribution to the elevated total RNA. We supposed that the reduced RNA degradation rate likely made a primary contribution to the rise of total RNA in later phases. Therefore, we calculated Spearman's rank correlations between newly transcribed RNA and total RNA of the genes that were upregulated post infection. Correlation of new versus total RNA showed a drift to high correlation at 6 and 12 h, and then declined at 24, 48 and 72 h (Fig. 3B and Supplementary Fig. 6B). We then presented fold changes of new RNA and total RNA and NTR for each gene. Many genes upregulated new RNA transcription at 6 and 12 h post infection compared to 0 h. Parallelly, these genes tended to possess higher NTR, suggesting that transcription contributed to a large part of the increased RNA levels (Fig. 3C and Supplementary Fig. 6C). In contrast, in the late phases of infection, new RNA transcription and NTR were declined. However, there were still many upregulated total RNA at that time points (Fig. 3C), suggesting that other factors exist to regulate total RNA levels besides transcription.

Next, we listed the upregulated genes at each time point upon *Salmonella* infection and ordered these genes into several clusters based on the total and new RNA expression pattern. As previously mentioned, expression patterns of new and total RNA were similar early post infection, but became more different in the later phases (Fig. 3D and Supplementary Fig. 6D). Genes related to inflammatory response (*Nfkbia*, *Il1rn*) and cytokines (*Il1b*, *Ccl5*) were highly expressed in both new and total RNA in the early phase (cluster 3 and 4 in batch 1, cluster 2 and 3 in batch 2). Genes related to antigen processing and presentation (*Stat1*, *Tap1*, *Tap2*) were highly expressed in both new and total RNA in the late phase (cluster 6 and 7 in batch 1, cluster

4 in batch 2). In contrast, genes related to membrane receptors (*Ccr1*, *Tlr4*), protein stability (*Usp3*, *Mkrn1*) were highly expressed in total RNA but not in new RNA at later phases (cluster 8 in batch 1 and cluster 5 in batch 2). We further analyzed GO pathways of new and total RNA that were upregulated post infection. As expected, Toll-like receptor (TLR), IL-1, and macrophage chemotaxis related signaling pathway were enriched both in new and total RNA in the early phase of infection. Meanwhile, protein stability, response to oxidative stress, cell death and phagocytosis related pathways were enriched in total RNA in a later phase, but not in new RNA (Fig. 3E and Supplementary Fig. 6E). We conclude that genes involved in different processes are modulated with distinct mRNA control strategies.

We next estimated the transcript kinetic parameters for each gene at different time points: new RNA transcription rate (α), RNA degradation rate (γ) and RNA half-life ($t_{1/2}$). As a typical representative, the pro-inflammatory cytokine *Il1b* and chemokine *Ccl4* had very similar expression patterns between new RNA and total RNA (Fig. 3F). The new RNA synthesis of *Il1b* and *Ccl4* was rapidly activated at early phase and rapidly declined subsequently. As for *Psmb9*, a proteasome gene, total RNA level gradually rose up along with minimal changes in new RNA synthesis, and its RNA half-life was dramatically lengthened upon infection (Fig. 3F). Besides these specific genes, we then explored whether transcription rates and RNA half-lives were different for the entire pathways at each time point post infection. We performed GO enrichment analysis on upregulated genes at 6 h and 72 h, and calculated the average transcription rates and RNA half-lives of upregulated genes included in GO. We found that the genes upregulated in the early phase were mainly concentrated in TLR and NF-κB signaling, response to TNF and IL-1 cytokines, and leukocyte activation and chemotaxis pathways with high transcription rates and short RNA half-lives. In contrast, the genes upregulated in late phase were mainly enriched in cell-cell adhesion, protein stabilization and phagocytosis, whose transcription rates were relatively low and RNA half-lives were relatively long (Fig. 3G and Supplementary Fig. 6F). In addition, due to the delayed and weaker variation of gene expression, data in batch 2 tended to present the expression change patterns in early phase (Supplementary Fig. 6A–C). Expression patterns of new and total RNA at 12 and 24 h in batch 2 were similar to the patterns at 6 and 12 h in batch 1 (Supplementary Fig. 6D, E). However, expression patterns at 72 h in batch 2 still, to some extent, followed the regulatory mode presented in batch 1 (Supplementary Fig. 6D-F). These data suggest that the coordination between RNA transcription and degradation regulates mRNA dynamics during infection. Genes with different functions utilize different strategies to regulate mRNA levels. Our findings are in line with several previous pioneering works[4,29].

It should be noted that due to the methodological limitations, such as the deviation of real labeling time (S⁴U diffusion and cellular uptake time) and the inherent constraints in S⁴U incorporation efficiency and T-to-C conversion rates, newly synthesized RNAs could not be completely identified and the calculated synthesis rates and RNA half-lives might deviate from the absolute physiological values. Moreover, for long-lived RNAs, it could be inaccurate to estimate their RNA half-lives with only 2 h of pulse labeling. In addition, genes with very low new RNA levels as well as long RNA half-lives could be more susceptible to the sequencing noise. It could not be ignored that these methodological limitations may affect our results, especially the estimated lengthened RNA half-lives in the late phase post infection. However, compared with all genes, those genes in cluster 8 actually did not all extremely distribute in the upper left corner in the scatter plot, where genes have very low labeled RNAs and long RNA half-lives. Many of genes in cluster 8 had high levels of new RNA with short RNA half-lives (Supplementary Fig. 7A). Thus, only sequencing noise could not explain the phenomena of lengthened RNA half-lives in the late infection phase that we found. Moreover, GO enrichment further reflected the biological significance of different functional genes
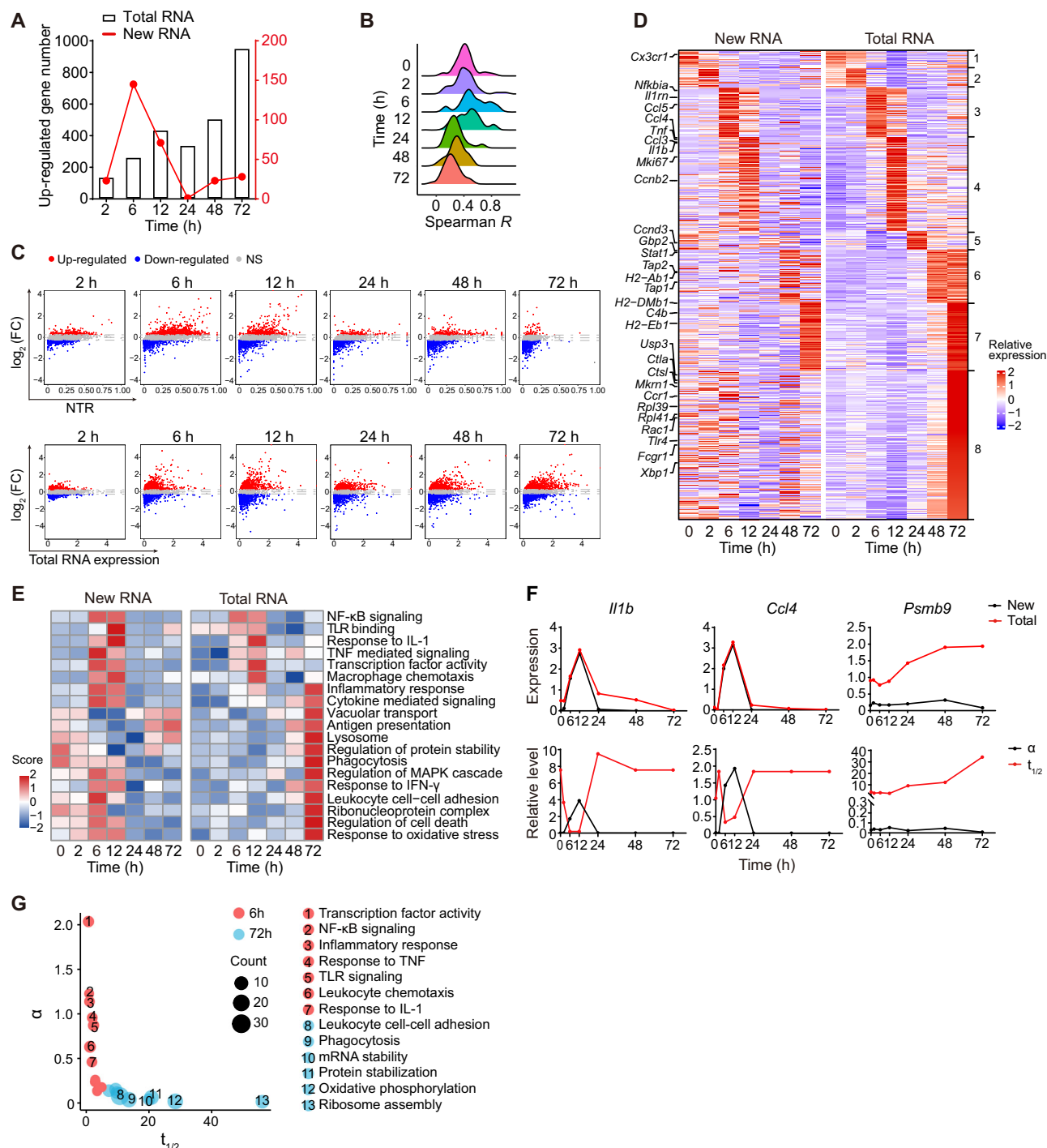
Fig. 3 | Different genes harbor various mRNA metabolic control strategies during immune response in macrophages. A Numbers of genes that upregulated (log$_2$ (fold change) > 0.25, p value < 0.05, Wilcoxon Rank Sum test) in new RNA and total RNA in macrophages at the indicated time points after infection compared with 0 h. **B** Ridgeline plot of new and total RNA expression correlations in macrophages. Genes highly expressed at the indicated time points were selected for Spearman's rank correlation analysis of new and total RNA. **C** Scatter diagrams showing NTR and fold change of new RNA in infected macrophages to new RNA in uninfected macrophages (top); total RNA expression and fold change of total RNA in infected macrophages to total RNA in uninfected macrophages (bottom). Red spots indicate upregulated genes (log$_2$(fold change) > 0.25); blue spots indicate downregulated genes (log$_2$(fold change) < −0.25); grey spots indicate no change. **D** Heatmap of new and total RNA expression pattern in macrophages at the indicated time points. Genes highly expressed at each time point were selected and

ordered into 8 clusters by their total RNA expression patterns, and rank of genes was mapped to new RNA. Expressions were scaled. **E** Heatmap showing enrichment scores of selected GO pathways in new RNA and total RNA at each time points post infection. **F** Line graph showing new and total RNA expression (upper) and new RNA transcription rate (α, normalized RNA counts per cells/h) and RNA half-life (t$_{1/2}$, h) (lower) of *Il1b*, *Ccl4* and *Psmb9* at each time point in macrophages. **G** Dot plot showing average new RNA transcription rate (α) and RNA half-life (t$_{1/2}$) of genes in GO pathways in macrophages. Genes significantly upregulated at 6 h or 72 h compared to 0 h were selected for GO enrichment analysis. Average values of α and t$_{1/2}$ of these upregulated genes in the indicated GO were calculated and shown in the dot plot. Each dot shows an average value of α and t$_{1/2}$ in a GO. The size of each dot represents the number of genes in the GO term. Source data are provided as a Source Data file.

adopting different regulatory modes (Fig. 3E, G and Supplementary Fig. 6E, F).

To confirm the RNA dynamics during infection, we generated pseudo-bulk datasets from our data and computed the RNA transcription and degradation rate and RNA half-life through the method in the TT-seq[30]. The conclusions were consistent between these two methods. Pro-inflammatory genes such as *Il1b* and *Ccl4* upregulated their transcription rates at the early phase after infection and then declined. Genes like *Psmb9* that upregulated at the late phase after infection did not obviously increase the transcription rate, but their RNA half-lives were dramatically extended (Supplementary Fig. 7B). Of note, the estimated RNA half-lives were biased since it takes about 10-20 min for the nucleoside analogs to enter into the cells in vivo (Supplementary Fig. 7C). Furthermly, our in vitro RNA metabolic labeling assay verified that *Salmonella* treated macrophages exhibited significantly prolonged *Psmb9* RNA half-life compared to untreated controls (Supplementary Fig. 7D).

Given that new-to-total ratios depended on both transcription and degradation rates, using NTR to describe the transcriptional state of cells might not be accurate. We normalized new RNA counts with total transcripts of non-responding genes (those genes that were not significantly upregulated or downregulated at any time points). We found that the plots of normalized labeled RNA were similar to the NTR plots previously shown (Supplementary Fig. 8A and Fig. 2A). In addition, we calculated the average rates of transcription and degradation in groups of genes (responders vs non-responders). Consistent with the previous findings, average transcription and degradation rates of responding genes were significantly increased at early stages (6 and 12 h) and then decreased at late stages (24, 48 and 72 h). By contrast, transcription and degradation rates of non-responding genes were relatively constant at different time points (Supplementary Fig. 8B and C).

RNA transcription and degradation rates change during immune response in neutrophils

Apart from macrophages, neutrophils are another innate immune cell type that act as the first responder to bacterial infection. Neutrophils harbor unique short lifespans and require constant replenishment from BM precursors. Neutrophils in BM are heterogeneous[31]. Using unsupervised graph clustering with the new RNA transcriptome, neutrophils were divided into three subsets: neutrophil precursors (preneutrophils), immature neutrophils and mature neutrophils. Under an uninfected state, new RNA transcription was higher in precursors and immature neutrophils than in mature neutrophils (Supplementary Fig. 9A). RNA velocity analysis showed developmental trajectory from precursors to mature neutrophils (Supplementary Fig. 9B). We found the signature genes highly transcribed in each subset were similar to the findings of previous scRNA-seq studies[32,33]. For example, the primary granule gene *Mpo*, proto-oncogene gene *Kit* and cell cycle gene *Cdk6* were highly transcribed in pre-neutrophils; secondary granule genes *Ltf* and *Ngp* were highly transcribed in immature neutrophils; and tertiary granule gene *Mmp8* and chemokine receptor *Cxcr2* were highly transcribed in mature neutrophils (Supplementary Fig. 9C). After *Salmonella* infection, mature neutrophils presented transcription activation, though the NTR in mature neutrophils was relatively low. Neutrophil precursors declined new RNA transcription at the early phase of infection (Supplementary Fig. 9D). Similar to macrophages, innate immune pathways such as TLR signaling and IL-1 response pathway were activated both in new RNA and total RNA in the early phase followed by decline (Supplementary Fig. 9E and F). In addition, some genes of neutrophil granule enzymes (*Cybb*, *Camp*) and neutrophil extracellular traps (*H3f3b*, *Hmgb1*) were also upregulated in the early phase and subsequently downregulated (Supplementary Fig. 9E). Of note, total RNA of genes related to phagocytosis and ribosome biogenesis reached a high level in a later phase while new RNA was

decreased at that time (Supplementary Fig. 9F), suggesting similar mRNA metabolic control strategies as in macrophages. Thus, we further calculated the transcription kinetic parameters of genes in mature neutrophils at each time point. Despite a similar variation tendency of new RNA and total RNA (upregulated at early phase and down-regulated at late phase), transcription rates of *Klf7*, *H3f3b* and *Ripor2* just mildly increased in the early phase (Supplementary Fig. 9G), which was different from the 'sharp' increased expression patterns of *Il1b* and *Tnf* in macrophages. This might be because new RNA transcription rate was lower and RNA half-life was longer in neutrophils than in macrophages. These genes might not be as strictly controlled as *Il1b* and *Tnf*. By contrast, total RNA of the ubiquitin ligase gene *Rnf8* was upregulated in a later phase post infection, which was due to extended RNA half-life. Altogether, the cooperation of new RNA transcription and RNA degradation regulates neutrophil response to bacterial infection.

Histone acetylation and m6A RNA methylation are changed after *Salmonella* infection

To reveal the mechanism underlying dynamic changes in RNA transcription and degradation during infection, we analyzed expression patterns of genes involved in regulating transcription and mRNA degradation. We found that many histone deacetylase genes (e.g., *Hdac1*, *Hdac2*, *Hdac3*, *Hdac4* and *Hdac6*) were obviously increased at late time points after infection, while the expression of *Crebbp* (a histone acetyltransferase and transcriptional coactivator) dramatically declined (Supplementary Fig. 10A). Histone acetylation is capable of marking genes for future activation and histone deacetylation is always linked to gene suppression[34]. We further confirmed the decrease of histone H3K27 acetylation after infection in both bone marrow and small intestines (Supplementary Fig. 10B and C).

In addition, for the prolonged RNA half-lives, we also noticed that expression of enzymes mediated m6A RNA methylation (e.g., *Mettl3* and *Mettl4*) was upregulated at late stages. On the contrary, the m6A eraser *Alkbh1* increased at the early stage and then decreased later. The variation of m6A RNA modification might affect the mRNA stability during infection[35] (Supplementary Fig. 10D). The changes of histone modification and RNA modification might represent either an active host countermeasure against pathogenic invasion or a passive result from pathogen-mediated regulatory manipulation of host cellular processes. We hypothesize that the dynamic alterations in cellular epigenome (e.g., histone acetylation) and epitranscriptome (e.g., m6A RNA modification) may be one of the mechanisms of RNA transcriptional and degradational regulation.

CD8+ T cells are initially activated early after *Salmonella* infection

The intestinal mucosa is the first line of defense against harmful pathogens, and large numbers of various immune cells colonize the intestine[36]. Thus, we detected new RNA and total RNA of intestinal immune cells after *Salmonella* infection. We surveyed early phases (2 and 6 h) and a late phase (72 h) to explore the initial activation of immune cells. In contrast to macrophages and DCs in BM, intestinal innate immune cells did not show obvious enhancement of transcription activity in response to infection and transcription rates were dramatically decreased at 72 h post infection (Fig. 4A and Supplementary Fig. 11A). We then inspected new RNA expression of genes with critical functions of each immune cell type. We noticed that pro-inflammatory cytokines (*Il1b*, *Il6*, *Tnf*) were not upregulated in early phases in macrophages and DCs (Fig. 4B and Supplementary Fig. 11B). GSEA analysis showed innate immune response in the gut was not elicited, and NF-κB signaling was even suppressed after infection (Supplementary Fig. 11C). In contrast, new RNA involved in response to interferon was upregulated in the early phases (Supplementary Fig. 11C). Therefore, we conclude that the innate immune response,

especially its pro-inflammatory role, was limited in the intestinal macrophages upon *Salmonella* infection.

Intriguingly, we noticed the elevated expression of T cell activation related genes (*Gzma, Gzmb, Ccl5, Nkg7*) as early as 2 h after infection (Fig. 4B). New RNA imaging confirmed the increased transcriptional activation in CD8+ T cells after infection (Fig. 4C and Supplementary Fig. 12A). GSEA of new RNA in CD8+ T cells showed an enrichment of immune response and activation of T cell-mediated cytotoxicity (Fig. 4D). Besides new RNA, the expression of total RNA of T cell activation related genes (*Gzma, Gzmb, Ccl4, Ccl5, Trbc2, Nkg7*) were also increased (Fig. 4E). Furthermore, *Gzma* and *Ccl5* were specifically and highly expressed in CD8+ T cells (Fig. 4F). Granzymes are a family of serine proteases that contain several members, including GzmA, GzmB, GzmH, GzmK and GzmM in humans. Granzymes cleave target proteins to induce target cell death through diverse, non-redundant pathways[36]. We found that *Gzma* and *Gzmb* were the two main components expressed in intestinal CD8+ T cells in mice (Supplementary Fig. 12B). Flow cytometry analysis showed that GzmA was much higher than GzmB (Fig. 4G). Compared with blood, most CD8+ T cells in the intestine highly expressed GzmA (Supplementary Fig. 12C). When cytotoxic lymphocytes recognize target cells and form immunological synapses, granzymes are then delivered into target cells to trigger cell death, leading to the elimination of transformed or infected target cells[37,38]. 3D imaging showed that *Salmonella* infection induced the expansion of GzmA expressing CD8+ T cells (Fig. 4H). In addition, many GzmA+ granules were released outside of CD8+ T cells upon infection (Fig. 4I). Collectively, GzmA expressing CD8+ T cells are initially activated in the intestine rapidly, only 2 h after bacterial infection, suggesting an innate-like quick response to an external stimulus.

IgA producing plasma cells rapidly expand after *Salmonella* infection

The intestinal mucosal barrier consists of mucus, antimicrobial peptides, and immunoglobulin A (IgA), separating the epithelium from both microbiota and pathogens in the lumen. In mammals, most IgA is produced by plasma cells residing in the intestine. Despite its abundance, the function of IgA still needs to be explored under homeostatic and disease conditions[39,40]. Thus, we analyzed the variation of new RNA transcription in intestinal B cells and plasma cells upon *Salmonella* infection. These two cell types from lamina propria were effectively separated with new RNA clustering (Supplementary Fig. 13A, B). RNA velocity analysis showed the development trajectory from B cells to plasma cells, and this trend was enhanced early after infection (Fig. 5A). In addition, plasma cell proportions were dramatically increased along with reduced B cell proportions at 72 h (Fig. 5B), indicating B cells differentiated into plasma cells upon *Salmonella* infection. Moreover, GSEA analysis with new RNA showed enrichment of immunoglobulin production and B cell activation gene sets at 72 h post infection (Supplementary Fig. 13C). Notably, IgA-producing plasma cells expanded after infection, while B cell numbers were reduced with flow cytometry analysis (Fig. 5C). We then analyzed the immunoglobulin repertoire of B cells and plasma cells at different time points. We observed that *Igha* was the main immunoglobulin expressed in plasma cells whereas B cells expressed *Ighm* and *Ighd* (Fig. 5D and Supplementary Fig. 13B, D). Total RNA of *Igha* in plasma cells was increased at 72 h post infection, whereas new RNA transcription was decreased, and the computed RNA half-life was extended (Fig. 5D and Supplementary Fig. 13D, E). In the early infection phase (2 and 6 h), total RNA co-expression of *Ighm* and *Ighd* was increased in B cells and then declined in the late phase (72 h) (Fig. 5D). Then we verified RNA levels of *Ighm* and *Ighd* with RT-qPCR and their protein levels with FACS. Although changes in protein seemed to lag behind RNA, these data showed similar variation trends that *Ighm* and *Ighd* in B cells were gradually upregulated till to

24 h after infection and then declined (Supplementary Fig. 13F and G).

IgA produced by plasma cells is transported into the enteric cavity through intestinal epithelial cells, where it protects against the adhesion of pathogens, blocks microbial antigens and neutralizes toxins, thereby assuring the homeostasis of intestinal microbiota and protecting the host from pathogen infection[41,42]. We noticed many more bacteria were coated by IgA after *Salmonella* infection (Fig. 5E). This coating by IgA antibody helps limit diffusion of intestinal luminal microbiota after epithelium damage[43]. In contrast, IgG coated bacteria showed no obvious change (Fig. 5E). Of note, we found IgA also coated *Salmonella* (Fig. 5F), suggesting IgA shows specificity to *Salmonella* antigens. Importantly, we found IgA-producing plasma cell numbers were much higher in the ileums of Crohn's patients than in those of healthy people (Fig. 5G), suggesting IgA+ plasma cells might be implicated in the regulation of human intestinal inflammation. Taken together, IgA-producing plasma cells rapidly expand at an early stage after *Salmonella* infection.

Intestinal epithelial cells rapidly transcribe immune factors upon *Salmonella* infection

The intestinal surface is covered with a single layer of intestinal epithelial cells (IECs) that form a physical barrier. IECs not only play an important role in nutrient absorption but also participate in resistance to intestinal bacterial invasion and maintenance of intestinal homeostasis. Various types of IECs have spatial distribution characteristics[44]. We found that the intestinal stem cells (ISCs) and transit amplifying (TA) progenitors in crypts actively transcribed new RNA at a steady state. New RNA levels of mature cells in upper villi were much lower (Supplementary Fig. 14A). Under *Salmonella* infection, new RNA transcription was rapidly enhanced in upper villus cells at early stage (2, 6 and 12 h), then lowered and restored to the uninfected state (24, 48 and 72 h) (Fig. 6A). These observations were verified by our scIVNL-seq data (Fig. 6B and Supplementary Fig. 14B). We noticed that late enterocytes obviously increased new RNA ratios at 6 h (Fig. 6B). We then determined new RNA transcription of functional genes that were upregulated post infection in each epithelial cell type (Fig. 6C and Supplementary Fig. 14C). Paneth cells are considered to be a primary source of various antimicrobial peptides that protect the host from bacterial infection[45]. However, we found new RNA transcription of lysozyme C (*Lyz1*) and α-defensins (*Defa22, Defa24*) in Paneth cells was even downregulated in early phase of infection (Fig. 6C and Supplementary Fig. 14D). However, some other types of antimicrobial peptides such as RegIII lectins (*Reg3b, Reg3g*) and *Lypd8* were highly transcribed and upregulated in enterocytes upon infection (Fig. 6C and Supplementary Fig. 14E). Lysozyme C and some α-defensins were highly expressed at 72 h, whereas Reg3b, Reg3g and Lypd8 were downregulated at that time (Fig. 6C, Supplementary Fig. 14E), suggesting dynamic expression of various antimicrobial peptides across IEC types is necessary for bactericidal effect.

Goblet cells secrete mucus to form a protective mucus layer to restrict the infiltration of food particles, digestive enzymes, and microorganisms. Muc2, a core component of mucus gel, was upregulated in goblet cells at 72 h post infection. In addition, goblet cells highly expressed chemokines *Ccl6* and *Ccl9* at 72 h (Fig. 6C and Supplementary Fig. 14C), suggesting a regulatory link with immune cells. Intestinal enteroendocrine cells (EECs) are specialized as sensory cells with neuron-like features. We found that EECs upregulated transcription of several neuropeptides and hormones (*Pyy, Gcg, Cck*) post infection (Fig. 6C and Supplementary Fig. 14C), suggesting that EECs might activate nerve cell-mediated defensive responses, such as reduced food intake, nausea and vomiting[46]. Intriguingly, Tuft cells highly transcribed several cytosolic nucleic acid sensors, including Zbp1 recognizing DNA in cytoplasm, Znfx1 sensing double-stranded RNA, and genes associated with RIG-I RNA sensors such as Oasl1 and
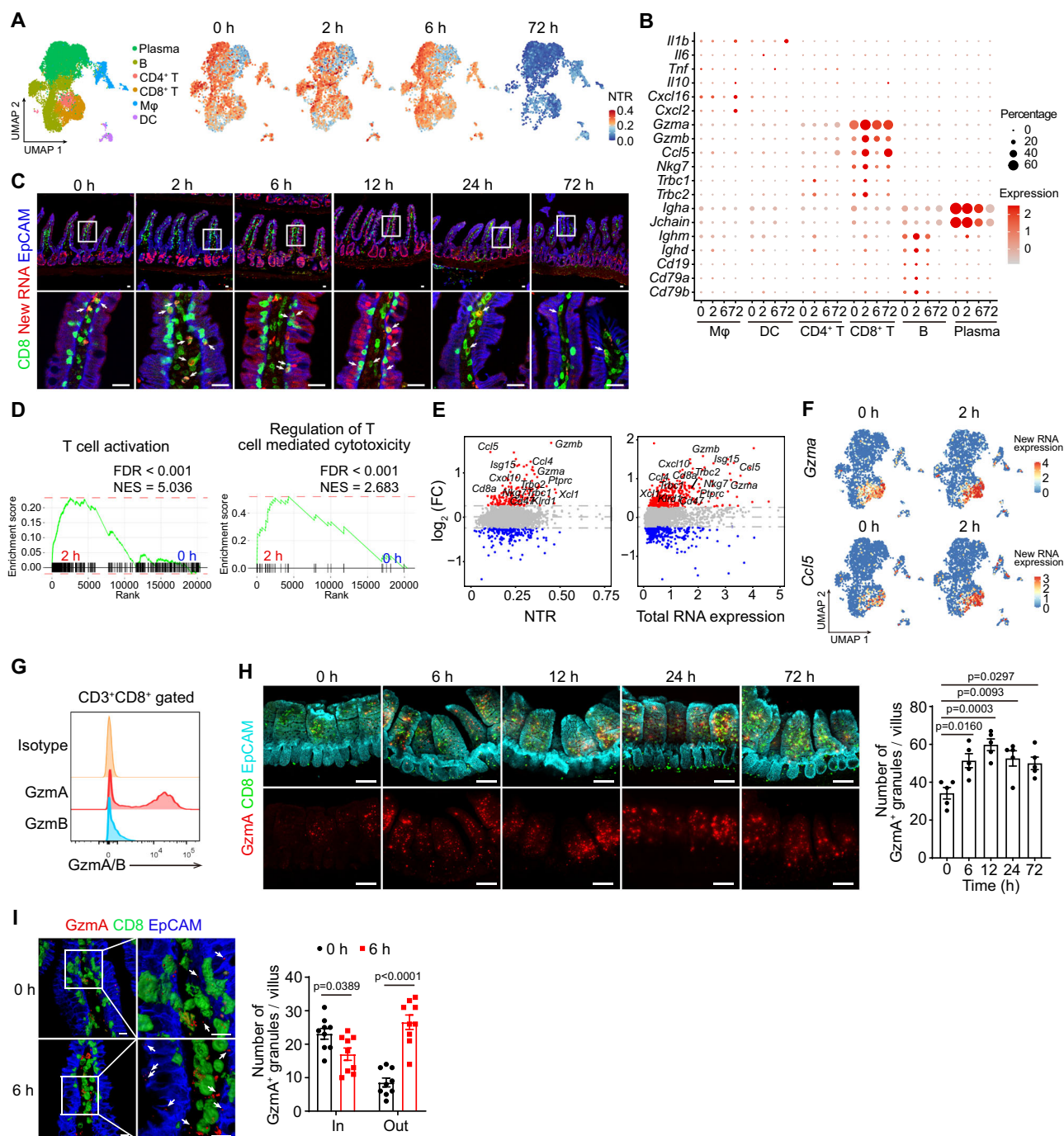
Fig. 4 | Intestinal CD8⁺ T cells are rapidly activated early after *Salmonella* infection. A UMAP plot showing cell type clusters of intestinal T cells, B cells, plasma cells and myeloid cells and their NTR at each time point post *Salmonella* infection. All cells from indicated time points were combined to identify cell types (left). NTR was overlaid on the UMAP plots (right). **B** Bubble plot showing log-normalized and scaled new RNA expression of genes. **C** New RNA (red) imaging of small intestine sections, co-stained with CD8a (green) and EpCAM antibodies (blue). Arrows denote new RNA signal positive CD8⁺ T cells. Scale bar, 20 μm. **D** GSEA analysis of new RNA in CD8⁺ T cells showing enrichment of indicated gene sets at 2 h post *Salmonella* infection (left) compared to 0 h (right). **E** Scatter plots showing fold change of new RNA (left) and total RNA (right) in CD8⁺ T cells between 2 h and 0 h. **F** UMAP plot showing new RNA expression of *Gzma* and *Ccl5* at 0 h and 2 h. Cell type defining of this UMAP plot was the same as in (**A**). **G** Flow cytometry analysis of GzmA and GzmB expression in CD8⁺ T cells. **H** 3D imaging of GzmA⁺ T cells at different time points post infection. GzmA (red), CD8a (green) and EpCAM (cyan) antibodies were stained. GzmA positive granules per villus are provided (right). Scale bar, 100 μm. *n* = 5 biologically independent replicates, 30 villi of each mouse for statistics. Results are shown as mean ± SEM. *p* values were determined by one-way ANOVA. **I** 3D imaging of GzmA⁺ T cells. Imaris surface rendering model of CD8⁺ T cells was built to estimate the inside and outside states of GzmA⁺ granules. Outside GzmA⁺ granules are indicated with arrows. Scale bar, 10 μm. *n* = 9 biologically independent replicates, 30 villi of each mouse for statistics. Results are shown as mean ± SEM. *p* values were determined by two-way ANOVA. Data in (**C**), (**G**), (**H**) and (**I**) are representative of at least three independent experiments. Source data are provided as a Source Data file.
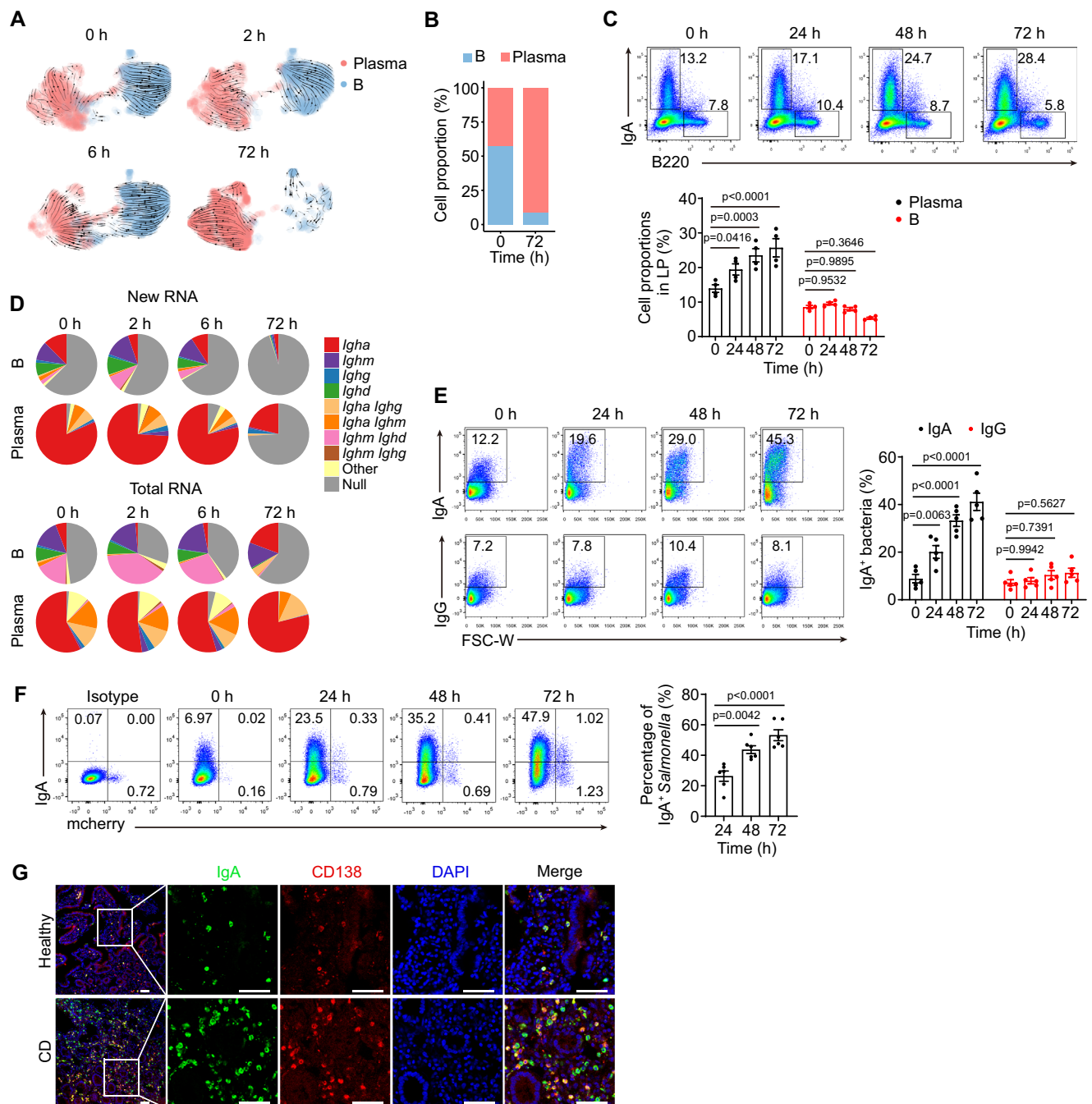
Fig. 5 | IgA-producing plasma cells quickly expand after *Salmonella* infection. **A** UMAP visualization of B cell and plasma cell development trajectory at each time point post infection. **B** Proportion of B cells and plasma cells at 0 and 72 h post *Salmonella* infection. **C** Flow cytometry analysis of IgA-producing plasma (IgA$^+$B220$^-$) and B cells (IgA$^-$B220$^+$). *n* = 4 biologically independent samples. Results are shown as mean ± SEM. *p* values were determined by two-way ANOVA. **D** Pie chart showing proportions of B cells and plasma cells expressing new RNA and total RNA of different immunoglobulin classes. Null, cells did not express *Igha*, *Ighg*, *Ighm* or *Ighd*. **E** Flow cytometry analysis of IgA and IgG coated fecal bacteria at each time point post *Salmonella* infection. *n* = 5 biologically independent replicates.

Results are shown as mean ± SEM. *p* values were determined by two-way ANOVA. **F** Flow cytometry analysis of IgA-coated mcherry expressing *Salmonella* in faeces at each time point post *Salmonella*-mcherry infection. Samples were mixed for isotype control. *n* = 6 biologically independent replicates. Results are shown as mean ± SEM. *p* values were determined by one-way ANOVA. **G** Immunofluorescence imaging of IgA production in human ileum samples of Crohn's disease patients and healthy people. IgA (green) and CD138 (red) antibodies were stained. Nuclei were counterstained with DAPI (blue). Scale bar, 50 μm. This image represents 39 ileum samples of Crohn's disease patients. Source data are provided as a Source Data file.

Ddx60 at a very early stage (2 h and 6 h) post infection (Fig. 6C and Supplementary Fig. 14C), suggesting Tuft cells might participate in innate recognition of invasive bacteria. Taken together, intestinal epithelial cells rapidly transcribe immune factors at an early stage upon *Salmonella* infection, which implies IECs are involved in the priming of immune response against bacterial infection.

Intestinal late enterocytes process and present *Salmonella* antigens to CD8$^+$ T cells for their early activation

Epithelial-immune cell crosstalk is essential for intestinal barrier homeostasis. We next performed a cell-cell communication analysis. Cell-chat analysis of ligand-receptor pairs between epithelial cells and immune cells showed that late enterocytes displayed strong
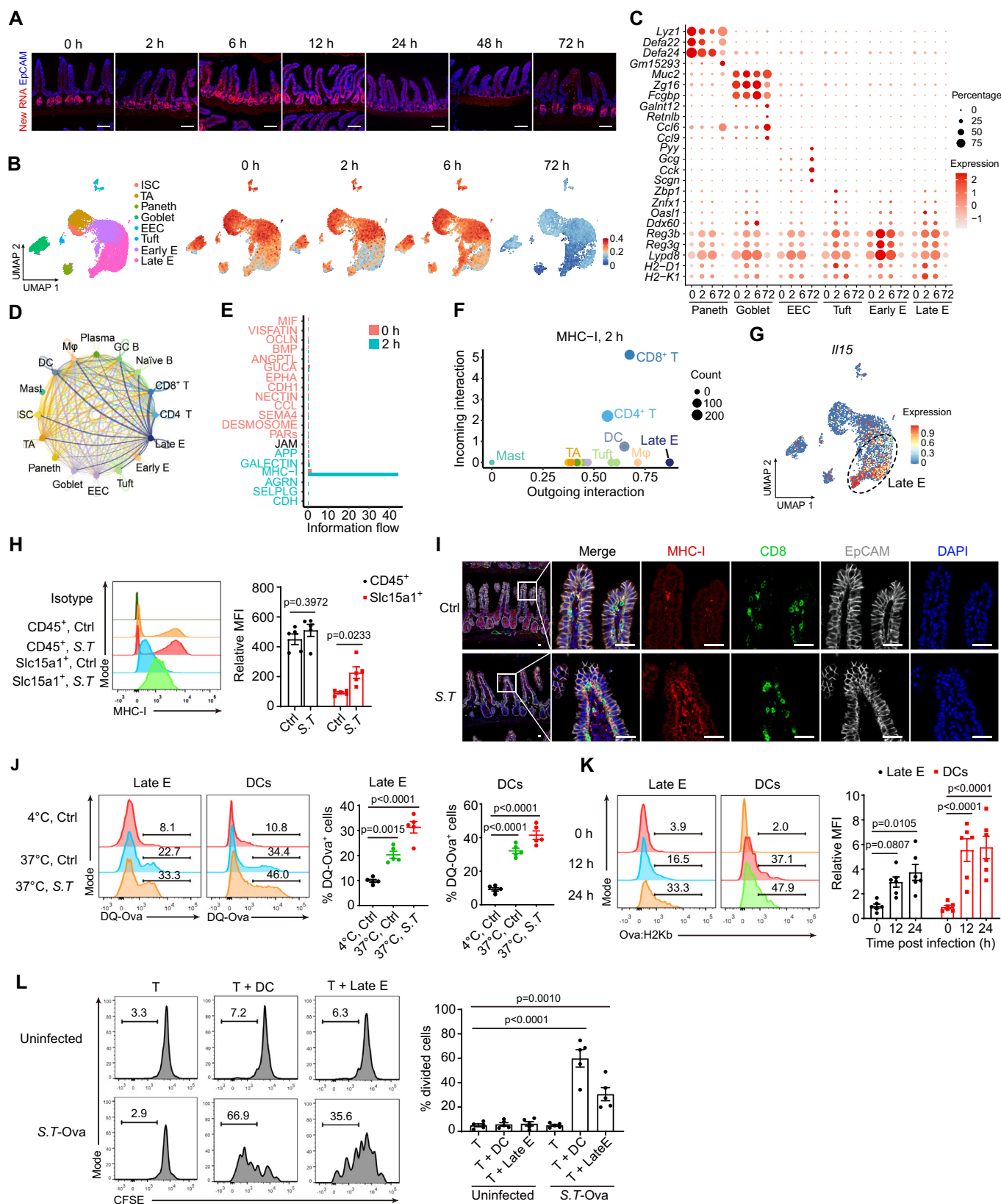
interaction with CD8^{+} T cells at 2 h post infection (Fig. 6D and Supplementary Fig. 15A). Furthermore, MHC-I was the most prominent signaling that was dramatically enhanced at 2 h post infection (Fig. 6E and Supplementary Fig. 15A). Through analysis of incoming and outgoing signals with each cell type, we observed that late enterocytes output MHC-I signaling, whereas CD8^{+} T cells received MHC-I signal

(Fig. 6F). Of note, outgoing of MHC-I signaling in the late enterocytes was even higher than that in professional antigen presenting cells such as DCs and macrophages (Fig. 6F).

Then we analyzed MHC-I expression in late enterocytes and found that MHC-I antigen presentation associated genes (*H2-D1, H2-K1, Tapbp, Tap1, Tap2*) were highly transcribed and upregulated in late

Fig. 6 | Intestinal late enterocytes process and present *Salmonella* antigens to CD8⁺ T cells for their early activation. A New RNA imaging of small intestines. Mice were infected with *Salmonella* and new RNA was labeled with EU (red). Scale bar, 100 μm. **B** UMAP plot of intestinal epithelial cells and NTR of each *Salmonella* infection time points. ISC, intestinal stem cell; TA, transit amplifying cell; EEC, enteroendocrine; E enterocyte. **C** Bubble plot showing log-normalized new RNA expression in IECs. **D** Intercellular communication network between IECs and immune cells at 2 h post *Salmonella* infection. Line width was proportional to the number of interactions. **E** Comparison of signaling pathways between 2 h and 0 h state based on the relative information flow. **F** Scatter plots showing outgoing and incoming interaction strength of MHC-I pathway at 2 h post infection. **G** Expression of *Il15* in IECs. Late E was marked. **H** Flow cytometry showing MHC-I expression in CD45⁺ immune cells and Slc15a1⁺ late E at 0 h and 6 h post *Salmonella* infection. Mean fluorescence intensities (MFI) were calculated. *n* = 5 biologically independent replicates. Results are shown as mean ± SEM. *p* values were determined by two-way ANOVA. **I** Immunofluorescence imaging of MHC-I expression in enterocytes and CD8⁺ T cells at 6 h post *Salmonella* infection. Scale bar, 50 μm. **J** Late E or DCs from uninfected or *Salmonella* infected mice (6 h) were sorted and incubated with DQ-Ova. DQ-OVA antigen processing ability was detected via flow cytometry. *n* = 5 biologically independent replicates. Results are shown as mean ± SEM. *p* values were determined by one-way ANOVA. **K** Flow cytometry analysis showing presentation of SIINFEKL-H2Kb complex in late E and DCs at each time points post *S.T*-Ova infection. MFI was calculated. *n* = 6 biologically independent replicates. Results are shown as mean ± SEM. *p* values were determined by two-way ANOVA. **L** Late E induced CD8⁺ T cell proliferation in vitro. Flow cytometry analysis showing CFSE signals of naive CD8⁺ T cells from OT-I mice that were cultured alone or co-cultured with late E or DCs from uninfected and *S.T*-Ova infected mice. *n* = 5 biologically independent replicates. Results are shown as mean ± SEM. *p* values were determined by one-way ANOVA. Results are representative of at least three independent experiments. Source data are provided as a Source Data file.

enterocytes at early stages post *Salmonella* infection (Supplementary Fig. 15B and C). In addition, GO analysis showed new RNA transcription enrichment of antigen processing and presentation pathway at 2 h post infection (Supplementary Fig. 15D). We also found new RNA transcription enrichment of IFN-γ signaling pathway post infection (Supplementary Fig. 15D), which is essential for the antigen presentation of colonic epithelial cells[47]. In contrast, organic hydroxy compounds, fatty acid metabolic process and organic anion transport pathways were obviously downregulated, suggesting late enterocytes suppressed nutrient absorption and transport function but enhanced immune function upon *Salmonella* infection. In addition, late enterocytes also highly expressed IL-15 (Fig. 6G), which is essential for the priming of CD8⁺ T cell activation and proliferation.

Based on the above observations, we supposed that late enterocytes might present *Salmonella* antigens to CD8⁺ T cells post *Salmonella* infection. We next identified that the oligopeptide transporter *Slc15a1* was specifically and highly expressed in late enterocytes (Supplementary Fig. 14B and Supplementary Fig. 15E). Late enterocytes were able to be isolated using Slc15a1 surface marker (Supplementary Fig. 15F). As expected, the upregulated expression of MHC-I molecules in late enterocytes post infection was further validated by flow cytometry (Fig. 6H) and immunofluorescent imaging (Fig. 6I). Of note, MHC-I molecules were mainly expressed on the basal membrane of late enterocytes (Fig. 6I), which was physically close to CD8⁺ T cells. We then sorted late enterocytes and tested their capacity to endocytose and process exogenous ovalbumin antigen. DQ-OVA, a self-quenching conjugate of ovalbumin, exhibits green fluorescence upon proteolytic degradation. We found that late enterocytes were able to process DQ-OVA, and *Salmonella* infection increased DQ-OVA processing ability (Fig. 6J). Interestingly, the antigen processing capacity of late enterocytes was similar to that of professional DCs (Fig. 6J). To explore whether late enterocytes could present bacterial antigens, we infected mice with ovalbumin expressing *Salmonella* (*S.T*-Ova) by gavage (Supplementary Fig. 15G). We noticed that late enterocytes could rapidly present Ova peptide-MHCI complex onto their surface at 12 h post *S.T*-Ova infection (Fig. 6K). We next tested whether late enterocytes could activate naive CD8⁺ T cells in an antigen-specific manner. We co-cultured naive CD8⁺ T cells that recognize the Ova₂₅₇₋₂₆₄-MHC-I complex from OT-I mice with late enterocytes or DCs from uninfected or *S.T*-Ova infected mice. We observed that late enterocytes from *S.T*-Ova infected mice could activate naive CD8⁺ T cell proliferation, whereas late enterocytes without *S.T*-Ova infection did not initiate naive CD8⁺ T cell proliferation (Fig. 6L). Treated DCs were used as a positive control. Altogether, intestinal late enterocytes express MHC-I molecules as well as process and present *Salmonella* antigens to activate CD8⁺ T cells at an early stage after *Salmonella* infection, serving as antigen presenting cells for priming of adaptive immunity against bacterial infection.

Discussion

Here we established the scIVNL-seq method to disentangle the new and total RNA of immune cells in vivo and resolve RNA dynamic changes upon *Salmonella* infection. Although gene expression is involved in the interplay of RNA transcription, processing and degradation, RNA abundance is still usually measured as a proxy for transcription activity, and current RNA-seq approaches miss information on real temporal dynamics. Our work has demonstrated that total RNA is not always in correspondence with new RNA transcription and that RNA transcription and degradation together orchestrate mRNA levels. Under homeostatic state, new RNA levels are much higher in stem and progenitor cells than in differentiated cells, both in BM and intestine. Most genes are silenced except for some functional genes in each mature cell. Indeed, chromatin in stem cells is considered to be more open and accessible compared to differentiated cells[48]. During lineage commitment and cell differentiation, chromatin architecture undergoes dynamic switch, which is essential for spatiotemporal regulation of key gene transcription[49]. The half-life of RNA is markedly variable among different genes. Thus, new RNA levels reflect more realistic information about chromatin openness and the transcription activation state compared to total RNA.

Upon *Salmonella* infection, BM macrophages rapidly elicit transcription activation and new RNA reaches a peak level in an early phase, followed by a reduction to the uninfected state. Of note, genes related to TLR, NF-κB signaling and pro-inflammatory cytokines IL-1β and TNF-α followed this transcription pattern. Both RNA transcription rates and degradation rates are high, and total RNA levels are strictly in line with new RNA. On the contrary, in the late phase post infection, even though new RNA transcription is decreased, total RNA of some genes related to phagocytosis, protein stabilization and ribosome assembly are still up-regulated. Therefore, we conclude that genes involved in complex processes that contain multiple steps and are sustained for a period of time tend to transcribe at a low rate with slow RNA degradation for integrating transcriptional information over time. Our data showed that RNA degradation and stability control are also essential to regulate mRNA levels besides RNA transcription. We revealed the mRNA metabolic control mechanism that guarantees a rapid and efficient response for eliminating external stimuli, and meanwhile avoiding persistent inflammation and excessive tissue damage. However, it should be noted that this metabolic labeling approach for in vivo single-cell new RNA detection has inherent methodological limitations, which may lead to inaccuracies in calculated RNA synthesis rates and RNA half-lives. Key contributing factors include temporal discrepancy between the labeling and actual RNA metabolic time (e.g., the time required for S⁴U diffusion and cellular incorporation, as well as inconsistent in vivo S⁴U concentrations), limited efficiency of S⁴U integration into new RNA resulting in incomplete labeling, and the susceptibility of half-life calculations

for low-abundance new RNAs to sequencing noise interference. Consequently, the RNA regulatory patterns observed in this study require further validations, and the functional investigations will help to elucidate the underlying molecular mechanisms.

Without RNA metabolic labeling, newly transcribed RNA can be identified by the presence of introns. Then, the RNA velocity can be estimated by distinguishing between unspliced and spliced RNAs in traditional single-cell RNA sequencing data. However, the RNA velocity estimated by this method has several critical limitations when applied to specific genes with no polyA/T-enriched intron regions or low expression. The conventional RNA velocity method treats transcription rates as a state-dependent constant, and the degradation rate constant is intrinsically scaled relative to the splicing rate, resulting in estimating relative velocity values rather than absolute quantities. By reconciling RNA metabolic labeling and intrinsic splicing kinetics, Dynamo overcomes the intrinsic limitations of conventional splicing-based RNA velocity and estimates accurate and absolute velocities by modeling transcription rates as a gene-/cell-dependent variable. Applying Dynamo to analyze our data accurately describes dynamic changes in transcription and degradation rates during the immune response to infection.

It is considered that innate immunity acts as the first defense line against enteric pathogen infection and is quickly activated within hours. However, which innate immune cells upon infection are initially activated is still unclear. Over infection, activation of T cells and B cells requires a period of time, usually a week[14]. In this study, we showed that BM macrophages are first primed at a very early stage upon infection. We noticed that the innate immune response in intestinal macrophages was limited compared with BM macrophages. *Il1b* and *Tnf* expression are not upregulated post infection, and NF-κB signaling is suppressed. In contrast, IFN signaling is early activated, which might be caused by *Salmonella* invasion into macrophages, leading to disturbance of the host transcriptome[25,50]. Importantly, intestinal CD8+ T cells are rapidly activated at an early stage, and T cell-mediated cytotoxicity genes such as *Gzma* are highly transcribed. Previous reports have shown that CD8+ T cells eliminate intracellular bacteria and parasites through perforin-mediated delivery of granzymes[51]. Whereas the lytic capacity of intestinal CD8+ T cells is weak in rectal CD8+ T cells compared to their blood counterparts[52]. How intestinal CD8+ T cells participate in killing intracellular *Salmonella* or clearing infected cells needs further investigation. In addition, we found that IgA-producing plasma cells rapidly expand at an early phase over *Salmonella* infection. We observed that IgA binds *Salmonella* bacteria, suggesting IgA shows specificity to *Salmonella* antigens. We conclude that *Salmonella* antigens elicit specific B cells to generate IgA-producing plasma cells, leading to specific IgA production. How B cells are activated by antigen presenting cells still needs further investigation.

Recent reports have showed that Lgr5+ ISCs present antigens and activate naive T helper cells via MHC-II[53]. Besides ISCs, MHC-II molecules are also expressed in other types of IECs. Food antigens induce MHC-II expression in IECs, which in turn induces Tr1 cells in the small intestine[54]. Intestinal microbiota also regulates MHC-II expression in IECs[55]. In addition, IFNγ sensing is required for antigen presentation by colonic epithelial cells to mediate the development of pathogenic CD4+ T cell responses[47]. Here, we found intestinal epithelial cells rapidly transcribe immune factors at an early stage upon *Salmonella* infection. However, how IECs are involved in the priming of the immune response against bacterial infection needs further investigation. We also observed that intestinal late enterocytes highly express MHC-I molecules and dramatically increase transcription of MHC-I genes rapidly after *Salmonella* infection. Late enterocytes are able to process and present *Salmonella* antigens to activate CD8+ T cells at an early stage after *Salmonella* infection. Therefore, late enterocytes serve as antigen presenting cells for the initiation of adaptive immunity at an early stage upon bacterial infection.

In summary, our findings show that new RNA levels reflect more realistic information about chromatin openness and the transcription activation state compared to total RNA. The interplay of new RNA transcription and degradation regulates the immune response process. BM macrophages are first primed at a very early stage upon *Salmonella* infection. The innate immune response in intestinal macrophages is limited compared with BM macrophages. Notably, intestinal CD8+ T cells and plasma cells are rapidly and specifically activated at the early stage post *Salmonella* infection, and late enterocytes serve as antigen presenting cells for the initiation of adaptive immunity. Our findings challenge the doctrine boundary between innate immunity and adaptive immunity against bacterial infection.

Methods

All experiments in this article comply with all relevant ethical regulations and are approved by the Institutional Committee of Institute of Biophysics, Chinese Academy of Sciences. All mice were housed under a specific pathogen-free environment, with 12 h dark/light cycle, 20 ± 2 °C, and 50% humidity conditions, and were used for experiments at the age of 8–10 weeks. The animal experimental protocols were approved by the Institutional Animal Care and Use Committee of Institute of Biophysics, Chinese Academy of Sciences.

Antibodies and reagents

FITC TNF-α (Cat# 11-7321-81, Clone# MP6-XT22, 1:100 for FC), PE IL-1β (Cat# 12-7114-80, Clone# NJTEN3, 1:100 for FC), eFluor450 CD11b (Cat# 48-0112-80, Clone# M1/70, 1:100 for FC), eFluor450 CD3 (Cat# 48-0032-80, Clone# 17A2, 1:100 for FC), APC-eFluor780 CD11c (Cat# 47-0114-80, Clone# N418, 1:100 for FC), FITC CD8a (Cat# 11-0081-81, Clone# 53-6.7, 1:100 for FC), PE GzmA (Cat# 12-5831-80, Clone# GzA-3G8.5, 1:100 for FC), PE GzmB (Cat# 12-8898-80, Clone# NGZB, 1:100 for FC), eFluor450 B220 (Cat# 48-0452-82, Clone# RA3-6B2, 1:100 for FC), FITC IgA (Cat# 11-4204-81, Clone# mA-6E1, 1:100 for FC), PerCP-Cyanine5.5 CD45.2 (Cat# 45-0454-80, Clone# 104, 1:100 for FC), eFluor450 CD45 (Cat# 48-0451-80, Clone# 30-F11, 1:100 for FC), PE-Cy7 IgM (Cat# 25-5890-80, Clone# eB121-15F9, 1:100 for FC), Percp-eFluor710 IgD (Cat# 46-5993-80, Clone# 11-26c (11-26), 1:100 for FC), eFluor450 CD326 (EpCAM) (Cat# 48-5791-82, Clone# G8.8, 1:100 for FC, 1:500 for IF), F4/80 (Cat# 14-4801-82, Clone# BM8, 1:500 for IF) and PE MHC Class I (H-2Kd/H-2Dd) (Cat# 12-5998-81, Clone# 34-1-2S, 1:100 for FC, 1:300 for IF) antibodies were purchased from Thermo Fisher Scientific. Alexa Fluor 647 CD31 (Cat# 102515, Clone# MEC13.3, 1:300 for IF), APC IgG1 (Cat# 406609, Clone# RMG1-1, 1:100 for FC), APC IgG2a (Cat# 407109, Clone# RMG2a-62, 1:100 for FC), APC IgG2b (Cat# 406711, Clone# RMG2b-1, 1:100 for FC), PE CD138 (Cat# 142503, Clone# 281-2, 1:100 for FC) and PE OVA$_{257-264}$-H-2Kb (Cat# 141604, Clone# 25-D1.16, 1:100 for FC) antibodies were purchased from BioLegend. Anti-Slc15a1 antibody was purchased from Abcam (Cat# ab203043, 1:300 for FC). Anti-Ovalbumin antibody was purchased from Proteintech (Cat# 67614-1-Ig, Clone# 1D3D5, 1:3000 for WB). 5-ethynyluridine (EU) (69075-42-9) and 4',6-Diamidino-2-phenylindole dihydrochloride (DAPI) (D8417) were purchased from Sigma-Aldrich. 4-thiouridine (S^{4}U) was purchased from Singleron Biotechnologies. DQ-Ovalbumin (D12053), Monensin Solution (1000X) (00-4505-51), 7-AAD (00-6993-50) and CellTrace CFSE Cell Proliferation Kit (C34570) were purchased from Thermo Fisher Scientific. IntestiCult Organoid Growth Medium (06005) was purchased from STEMCELL Technologies

Animals and Crohn's disease samples

All mice were C57BL/6 background and were kept under specific pathogen-free conditions. Routine random sampling of mice is performed through serological testing, microbial culture, and histopathological examination to ensure pathogen-free status. To confirm the absence of *Salmonella* in SPF conditions, we collected fecal samples, extracted microbial DNA, and performed quantitative PCR

targeting the Salmonella-specific invA gene. OT-I and Lgr5-EGFP-IRES-creERT2 mice were purchased from The Jackson Laboratory. Male and female mice aged 8 to 10 weeks were used. Human resected ileum tissues were obtained from the Sixth Affiliated Hospital, Sun Yat-sen University (Guangzhou, China) with informed consent, according to the Institutional Review Board (IRB) approved protocol.

S⁴U in vivo labeling and cell dissociation

S^4U in vivo labeling and scIVNL-seq processes were shown in Fig. 1a. The schematic diagrams were created using Adobe Photoshop (Version 22.0.0) or Adobe Illustrator (Version 25.0.0). In brief, mice were administrated with S^4U (1% of body weight) through tail vein injection. 2 h later, mice were euthanized. Femurs and small intestines were collected. For collecting BM cells, muscles from the femurs were removed, and epiphyses of the bones were cut off. BM cells were flushed out from the femurs using a 12 cc syringe filled with ice-cold RPMI culture medium. Red blood cells were lysed with red blood cell lysis buffer (eBioscience), and BM cells were washed twice with ice-cold PBS. In order to collect epithelial cells and immune cells in the intestinal lamina propria, Peyer's patches were removed. Then intestinal tissues were opened longitudinally and washed four times with ice-cold PBS to remove intestinal contents and mucus. Tissues were cut into small pieces and then incubated in digestive buffer (SCelLiVe Tissue Dissociation Kit, Singleron Biotechnologies) at 37 °C with shaking at 100 rpm. Samples were vigorously pipetted every 5 min. 30 min later, the single-cell suspension was passed through a 40 μm filter. Red blood cells were lysed, and cells were washed twice with ice-cold PBS.

scIVNL-seq library preparation

We used DynaSCOPE™ Single Cell Dynamic RNA Library Kit (Singleron Biotechnologies) to construct scIVNL-seq libraries according to the operating manual. Briefly, small intestine tissues were isolated and dissociated into single cells after S^4U labeling. Single-cell suspension was loaded onto microwell chips for single cell partition, followed with bead loading and cell lysis. After 20 min incubation at room temperature (RT), mRNA in each well was captured on a magnetic bead coated with oligonucleotides, each containing a primer sequence, a cell barcode, a unique molecular identifier (UMI), and a poly-T tail. After collecting all beads that captured mRNA, S^4U integrated into the new RNA was converted into cytidine analogs. mRNA was incubated with the conversion reagent at 25 °C for 60 min. Mutations were inserted at the indicated sites on reverse transcription. For reference control samples, mRNA was incubated under the same conditions but without the conversion reagent. The reverse transcription reaction was incubated at 42 °C for 90 min. cDNA amplification was performed by PCR using 13 cycles. PCR amplification products were purified using AMPure XP beads. After cDNA fragmentation and adaptor ligation, products were purified and amplified by PCR. After size selection, libraries were sequenced on the Novaseq 6000 with 150 bp paired end reads.

Immunofluorescence imaging and New RNA imaging

EU (150 mg/kg) was injected into mice via tail vein injection. 2 h later, femurs and small intestines were collected. Femurs were fixed with 4% paraformaldehyde (PFA) (Sigma) at room temperature for 12 hours. Then femurs were decalcified in decalcifying buffer (10% EDTA in PBS, pH 7.4) for 72 h, changing new decalcifying buffer every 24 h. Intestinal samples were coiled into a 'Swiss roll' and fixed with 4% paraformaldehyde (PFA) (Sigma) at RT for 2 h. Tissues were dehydrated with 30% sucrose in PBS at 4 °C overnight. Then, samples were embedded in OCT compound (Tissue-Tek) and stored at −80 °C before sectioning (8 μm) on a Cryostat (Leica). For immunofluorescence staining, sections were permeabilized in PBS containing 1% Triton X-100 for 30 min at RT, followed with blocking with 10% BSA for 30 min at 37 °C. Primary

antibodies were diluted with PBS containing 1% BSA, and sections were incubated with primary antibodies on a shaker at 4 °C overnight. Then sections were washed 3 times with PBST (0.05% Tween-20 in PBS), 5 min each, and then were incubated with secondary antibodies and DAPI for 1 h at RT. Sections were then washed 3 times with PBST. For new RNA imaging, EU integrated into new RNA were covalently linked with Alexa Fluor 594 via copper-catalyzed click reaction using the Click reaction kit (Beyotime Biotech Inc). Samples were imaged using the confocal laser scanning microscope (A1R⁺, Nikon) or the all-in-one fluorescence microscope (BZ-X800LE, KEYENCE). Imaging was analyzed with Imaris 9 software.

Bacterial strain

Salmonella Typhimurium (SL1344) was from the Institute of Microbiology, Chinese Academy of Sciences. For mCherry-expressing *Salmonella Typhimurium* (S.T-mcherry) and Ovalbumin-expressing *Salmonella Typhimurium* (S.T-Ova) construction, mCherry and Ova expression cassettes promoted by the Tac promoter were cloned into the pBBR1MCS2 vector. Then pBBR1MCS2-Tac-mCherry and pBBR1MCS2-Tac-Ova vectors were transfected into *Salmonella* respectively via electransfection. Briefly, *Salmonella* was aerobically cultured in Luria Broth (LB) medium at 37 °C temperature on a shaker (220 rpm) overnight and 3 ml bacteria solution was centrifuged at 4 °C for 10 min at 3000 g. Then discard the supernatant, and the bacterial pellet was resuspended with 5 ml ice-cold sterile ddH₂O and centrifuged. Repeat wash with 5 ml ice-cold sterile H₂O containing 10% glycerin for three times and finally resuspended the bacterial pellet thoroughly in 100 μl ice-cold sterile H₂O containing 10% glycerin. 2 μg of plasmid DNA was added in to 100 μl bacterial suspension and mixture was transfered into a pre-cold, sterile 0.2 cm gap cuvette. Insert the cuvette into the MicroPulser electroporator (BIO-RAD) and electroporate at 1.8 kV, 25 μF for 5 ms. The cell suspension was quickly recovered by resuspending into 1 ml LB medium and incubated at 37 °C for 30 min. Then bacteria were plated onto LB agar plates with kanamycin. Plates were incubated at 37 °C for 17 h. mCherry fluorescence of *Salmonella* clones was checked with fluorescence microscope (Nikon). Ovalbumin expression was checked by western blot.

Salmonella infection

Salmonella infection was performed as previously described[56]. In detail, 8-10 week old mice were deprived of food and water for 4 h. Then mice were gavaged with 20 mg streptomycin sulfate in 200 ml PBS. 24 h later, mice were again deprived of food and water for 4 h, and then were gavaged with 10^8 CFUs of *Salmonella*. Samples were collected at the indicated time points after *Salmonella* infection. We gavaged mice with sterile PBS buffer (the carrier of Salmonella suspension) as the 0-time point. Other operations (such as 4 h starvation and streptomycin pretreatment) were kept consistent with the Salmonella infection group.

Flow cytometry

BM cells were flushed out with ice-cold PBS. Red blood cells were lysed with red blood cell lysis buffer, and BM cells were washed twice with ice-cold PBS. For flow cytometry analysis of the whole intestinal epithelial cells and immune cells, small intestines were cut open longitudinally, and Peyer's patches were removed. Intestines were cleaned and cut into small pieces and incubated in digestive buffer (SCelLiVe Tissue Dissociation Kit, Singleron Biotechnologies) at 37 °C with shaking at 100 rpm for 30 min. Samples were vigorously pipetted every 5 min. Then the single-cell suspension was passed through a 40 μm filter. Red blood cells were lysed, and cells were washed twice with ice-cold PBS. To collect the immune cells in lamina propria (LP), epithelial layers were removed by incubation three times in 5 mM EDTA Ca²⁺ and Mg²⁺ free Hank's medium for 20 min each at 37 °C, and the epithelial cells were collected if needed. Then, intestines were cut into

pieces and digested twice for 40 min each at 37 °C with Collagenase II and III (1 mg/ml; Worthington), DNase I (200 mg/ml; Roche) and dispase (4U/ml; Sigma). Mononuclear cells were isolated with 40%–80% Percol gradient, and washed twice. Isolated cells were blocked with anti-CD16/32 antibody for 30 min on ice. Cells were then stained with surface markers for 45 min on ice. 7-AAD was stained for 10 min before analysis to exclude dead cells. For cytokine analysis, cells were incubated with Monensin for 4 h at 37 °C. Cells were fixed and permeablized by Intracellular Fixation & Permeablization buffer set (eBioscience) after surface marker staining, followed by staining with antibodies against intracellular antigens for flow cytometer (FACS Aria III, BD). FlowJo v10 (TreeStar) was used to analyze flow cytometry results.

Antigen processing and presentation

For the antigen processing assay, mice were infected with *Salmonella*. 6 h later, small intestines from uninfected and infected mice were collected and dispersed into single cells. 5×10^4 CD11c$^+$ DCs and 5×10^4 EpCAM$^+$Slc15a1$^+$ intestinal late enterocytes were sorted. Cells were cultured with 10 mg/ml DQ-Ovalbumin at 4 °C or 37 °C for 2 h, and then were washed and analyzed via flow cytometry.

For the antigen presentation assay, mice were infected with Ovalbumin-expressing *Salmonella* (*S.T*-Ova). At the indicated time points, small intestine tissues were collected and dispersed into single cells. Intestinal DCs (CD11c$^+$) and late enterocytes (EpCAM$^+$Slc15a1$^+$) were analysed for the presentation of H2Kb:Ova complex on the surface detected by PE-conjugated H-2Kb-OVA$_{257-264}$ antibody via flow cytometry. For naive CD8$^+$ T cells in vitro activation, 5×10^4 intestinal DCs or 5×10^4 intestinal late enterocytes from *S.T*-Ova infected and uninfected mice were sorted. 5×10^4 naive CD8$^+$ T cells were sorted from the spleen in OT-I mice. Naive CD8$^+$ T cells were stained with 5 μM CFSE at 37 °C for 20 min, and then washed with complete culture medium to quench dye remaining in the solution. DCs or IECs were co-cultured with naive CD8$^+$ T cells in the organoid culture medium. Naive CD8$^+$ T cells only sample and naive CD8$^+$ T cells treated with heat killed *S.T*-Ova sample were as control. 3 days later, cells were stained with anti-CD8 antibody, and cell proliferation was analyzed by detecting the attenuation of the CFSE fluorescence intensity via flow cytometry.

scIVNL-seq data preprocessing

Paired-end sequencing reads of scIVNL-seq were processed to generate gene expression profiles using the scIVNL-seq pipeline (https://github.com/singleron-RD/CeleScope/blob/master/doc/assay/multi_dynaseq.md). Briefly, raw reads were processed with fastQC and fastp to remove low quality reads, such as those without poly T tails, cell barcode and UMI. Adapters and poly A tails were trimmed by Cutadapt before aligning paired reads to the mouse reference genome (GRCm38 with ensemble version 92 gene annotation) using STAR (version 2.5.3a). We then acquired gene counts and UMI counts by assigning uniquely mapped reads to genomic features with FeatureCounts (version 1.6.2). To quantify S^{4}U labeled and unlabeled reads, we got T-to-C substitutions in each read. Sites with background T-to-C substitutions (present in the reference sample without T-to-C conversion treatment) were determined and excluded for T-to-C substitution identification. Reads with the same cell barcode, UMI and gene were grouped together to count the numbers of labeled and unlabeled UMIs for each gene per cell. A UMI/transcript was defined as labeled (new RNA) if there was at least one T-to-C substitution in any one of the reads linked to the same UMI index (even if there existed reads, with the same UMI covering other cDNA fragments, that did not have T-to-C substitution). If the reads with the same UMI did not have any T-to-C substitution, then this UMI/transcript was identified as unlabeled (old RNA). By categorizing UMIs as either labeled or unlabeled for each gene within each cell, we assigned two distinct expression values to each gene: one that

corresponded to the count of new RNAs, and another that corresponded to the count of old RNAs. Consequently, for each sample, we generated two separate gene expression matrices: one detailing the new RNA counts and the other detailing the old RNA counts. Total RNAs were calculated as the sum of new RNAs and old RNAs.

Estimation of fractions of newly synthesized transcripts

Metabolic labeling strategies cannot generally label all new RNA in a single cell with S^{4}U. We implemented a binomial mixture model-based statistical correction strategy to adjust the observed fractions, which has been adapted for scSLAM-seq, NASC-seq and scNT-seq datasets[2,7,13]. In brief, the probability of observed number of T-to-C substitutions y_i for each gene transcript i containing n_i possible substitution positions are based on the following function:

$$f(\theta, p, q) = \theta \text{Binom}(y_i; p, n_i) + (1 - \theta)\text{Binom}(y_i; q, n_i) \qquad (1)$$

where θ is the estimated fraction of new transcripts in each gene, q is the background T-to-C mutation rate that is estimated the fraction of T-to-C mismatches in a paired control sample and p is the T-to-C substitution rate introduced by metabolic labeling in new transcripts.

The Expectation-Maximization algorithm described in the previous work[57] was implemented to estimate the parameter p by constructing a sparse matrix A where each element a$_{k,n}$ is the number of reads with k T-to-C conversions and n T bases in the genomic region that each read aligns to. This setup allowed us to test the Null hypothesis that the background T-to-C mutation rate q < p using a Binomial test on k-$Binom(n, q)$. For a specific combination of k and n, if the expected value calculated based on the background mutation rate q exceeds the threshold multiplied by the current element value, that is, $e_{k,n} > 0.01*a_{k,n}$, the proportion of unlabeled RNA in the reads at that position is considered too high and can be excluded. For each n and k we computed:

$$e_{k,n} = B(k; n, q) \cdot \sum_{k'} a_{k', n} \qquad (2)$$

During the iterations of the EM algorithm, this operation is performed only on those indices that have passed the above preliminary screening.

Then the Bayesian inference approach was employed to directly estimate fractions of new RNA. The estimated fraction of new reads θ is derived from the generative model built in the STAN modeling language (the STAN model code can be viewed in NASC-seq pipeline[13], https://github.com/sandberg-lab/NASC-seq/blob/master/data/NASCseqModel.stan). The STAN model defines the prior distribution that θ follows the Beta distribution. And the model uses binomial distribution to describe the probability of observing a specific number of conversions under a given substitution probability (p) and background substitution rate (q). In order to realize the Bayesian inference of this model, the proportion of labeled RNA are estimated through Markov Chain Monte Carlo (MCMC) method. Last, α defined as a ratio between labeled and estimated fractions of new transcripts was calculated to correct new RNA count matrix. In detail, α is defined as the average estimated detection rate of all genes for each cell with the constraint α < 1. The correction is applied by adjusting the counts of new RNAs based on the ratio α. For each gene in the cell, the new RNA level is determined by selecting the minimum value between the total RNA count and the number of labeled transcripts for that gene divided by α.

All steps above are performed using the code from statistical estimation procedure of dynast (https://github.com/aristoteleo/dynast-release) described in the Dynamo study[28] and scNT-seq pipeline[13] (https://github.com/wulabupenn/scNT-seq/).

Quality control of scIVNL-seq

Seurat R package (version 4.0.6) was used to generate Seurat objects from result files pre-processed by scIVNL-seq pipeline. Then we chose the quickPerCellQC function in Scater R package (version 1.18.5) to filter low-quality cells whose feature counts, numbers of expressed features, percentages of mitochondrial genes, percentages of ribosomal genes or percentages of dissociation genes fell beyond 3 Median Absolute Deviations (MADs). Cells with <200 genes or > 5000 genes were also removed. Additionally, doublet detection and removal were performed with software scDblFinder (version 1.13.6), and cells with scDblFinder.class annotation defined as singlet were finally entered into following analysis (Supplementary Data 1).

Data normalization

After quality filtering, all Seurat objects of bone marrow samples were merged into a *Salmonella* infection time series (0, 2, 6, 12, 24, 48 and 72 h) object. All Seurat objects of small intestine (SI) samples (0, 2, 6 and 72 h) were merged into two main Seurat objects according to cell types (epithelial cells and immune cells). For normalization, total RNA count matrices of the merged Seurat objects were scaled by library size (total UMI counts), multiplied by 10,000 and transformed to log space (ln(gene total count*10000/library size +1)) using function NormalizeData with the parameter method = "LogNormalize". The new RNA count matrices were then normalized using the formula ln(gene total count*10000*NTR/library size +1). NTR was denoted as the ratio of new to total RNA.

Cell-type clustering and identification

For cell-type clustering, highly variable genes (HVGs) were identified using function FindVariableFeatures in Seurat. Expression levels of HVGs were scaled by function ScaleData before subjecting to Principal component analysis (PCA). Then Harmony[58] (https://github.com/immunogenomics/harmony), an algorithm that aligns cells into a shared embedding from different batches, was used to correct batch effect. RunHarmony function was performed to integrate data. For Seurat objects of BM and SI immune cells, most significant 30 harmony dimensions were selected and used for Uniform Manifold Approximation and Projection (UMAP) projection. Next, we used function FindCluster in Seurat with the parameter resolution = 2 to cluster cells. DimPlot function was used to visualize cells in the first two UMAP dimensions.

For cell-type identification, we used function FindMarkers in Seurat to calculate clusters specific genes via differential expression. we used the following canonical cell markers to identify the cell type: *Cd34, H2afy, Kit* for HSPCs; *Csf1r, Ccr2, Klf4* for monocytes; *Adgre1, Adgre4, Apoe* for macrophages; *Ly6g, S100a9, Ltf* for neutrophils; *Prss34, Mcpt8, Cpa3* for basophils; *Klrb1c, Ncr1, Klrd1* for NK cells; *Itgax, Siglech, Ctsl* for DCs; *Cd3d, Cd3e, Cd3g* for T cells; *Cd8a, Ccl5, Gzma* for CD8^{+} T cells; *Vpreb3, Chchd10, Ebf1* for pre B cells; *Cd79a, Cd79b, Cd19* for B cells; *Igha, Jchain, Igkc, Mzb1* for plasma cells; *Epcam* for all intestinal epithelial cells; *Lgr5, Ascl2, Olfm4, Axin2* for intestinal stem cells (ISCs); *Mki67, Cdk4, Pcna, Hmgb2* for TA cells; *Lyz1, Defa22, Defa24, Ang4* for Paneth cells; *Muc2, Tff3, Agr2, Zg16* for Goblet cells; *Dclk1, Trpm5, Gfi1b, Il25* for Tuft cells; *Chga, Chgb, Tac1, Neurog3* for Enteroendocrine cells (EECs); *Krt19, Fabp1, Reg3g* for early Enterocyte cells (early E); *Fabp6, Ada, Apoa4, Krt20* for late Enterocyte cells (late E). Erythroid cells and erythroblast cells in bone marrow were removed. We used function VlnPlot, FeaturePlot and DotPlot in Seurat to verify the specific expression of those marker genes in the identified cell types. Average gene expressions of total and new RNA in all cell types were provided in Supplementary Data 2-4.

Metabolic labeling-based RNA velocity analysis

Scanpy (version 1.9.1) and Dynamo (version 1.2.0) were employed for RNA velocity analysis. Normalized total RNA matrix and new RNA

matrix were used as data input for downstream analysis. We conducted the analysis following the standard Scanpy workflow, resulting in scaled data and identification of 2000 highly variable genes. From these 2000 genes, we selected the top 1250 genes based on new RNA expression levels. Scaled data and selected genes were used for subsequent preprocessing in Dynamo. Next, we followed a standard Dynamo workflow, which included generating streamline plots of velocity vectors in PCA space. Specifically, we set the parameter 'experiment_type' = 'one-shot', maintain_n_top_genes = True and geneset for parameter 'genes_to_use' and 'n_top_genes' in 'dyn.pp.recipe_monocle', while keeping all other parameters at default in the 'dyn.tl.dynamics', 'dyn.tl.reduceDimension' and 'dyn.tl.cell_velocities'.

Estimation of RNA half-life, RNA synthesis and degradation rate

We used Dynamo[7,28] (version 1.1.0) to estimate RNA half-life ($t_{1/2}$), RNA synthesis (α) and degradation rate (γ). Normalized total RNA matrix and new RNA matrix were used as the data input. The dyn.pp.recipe_monocle module was used to perform the preprocessing steps. Then, dyn.tl.dynamics was used to estimate RNA half-life, processing and degradation rate with default parameters. Detailed description of this algorithm is available at (https://github.com/aristoteleo/dynamo-release).

Differential expression analysis

After cell types were determined, cluster-specific genes were identified with the function FindAllMarkers in Seurat using Wilcoxon rank-sum test. Differential expression analysis between different time points of *Salmonella* infection (2, 6, 12, 24, 48 and 72 h) and non-*Salmonella* infection (0 h) control were performed with the FindMarkers function in Seurat using Wilcoxon rank-sum test. The threshold of bonferroni adjusted P value for differential expression upon *Salmonella* infection in each time point was set to 0.05. Additional requirements for differential expression included genes expressed in more than 25% of cells in a cluster (min.pct = 0.25) and with average $\log_2$ (Fold Change) > 0.25. New RNA transcripts with parameters min.pct = 0.1 and logfc.threshold = 0.25 were considered to be differentially expressed.

Spearman correlation analysis

To characterize the relationship between newly transcribed RNA and total RNA of genes that were specifically highly expressed at each time point post infection, we calculated the differentially expressed genes (DEGs) at all time points. Then we took the highly expressed DEGs at a certain time point as a group to calculate the Spearman's rank correlation between the new RNA and total RNA of the genes in the group. Differentially expressed genes were selected by applying the fold change cutoff of 1.5. Spearman's rank correlation analysis was performed with Hmisc R package (version 4.7-0).

GO enrichment analysis and Gene set enrichment analysis

Gene Ontology (GO) enrichment analyses examining significantly changes of cellular formation, biological processes and molecular functions in different time points of *Salmonella* infection were performed using clusterProfiler R package (version 3.18.1). Significant differentially expressed genes (DEGs) between control (0 h) and *Salmonella* treated samples (2, 6, 12, 24, 48 and 72 h) were calculated. We then converted gene symbols of gene sets into ENTREZ ID and performed GO enrichment pathway analysis through the enrichGO function. We mainly focused on enrichment results of Biological Process (BP) in which pathways with Benjamini Hochberg (BH) adjusted P values less than 0.05 were considered as significantly enriched. Gene Ontology (GO) pathway scores were calculated using the function AddModuleScore in Seurat (version 4.0.6). To estimate the average RNA half-life ($t_{1/2}$) and RNA synthesis rate (α) of genes in the indicated GO pathways (Fig. 3G), upregulated DEGs at 6 h or 72 h compared to

0 h were selected for GO enrichment analysis. Then average values of α and $t_{1/2}$ of genes in the indicated GO were calculated and shown in the dot plot. Each dot shows an average value of α and $t_{1/2}$ in a GO, and the size of each dot represents the number of genes associated with the GO term.

Gene set enrichment analysis (GSEA) was performed using the fgsea R package (version 1.16.0). Genes were ranked according to area under the receiver operator curve (AUC) calculated by the wilcoxauc function. MSigDB mouse gene sets were imported using the msigdbr R package (version 7.5.1). GSEA was performed using the fgsea function. Specifically, we set the parameter eps = 0 in the fgsea function. GSEA results were displayed using the plotEnrichment function.

Cell-cell communication
Based on cell types annotated in each sample, we used CellChat (version 1.1.3)[59] to analyze cell-cell communication and identified major signaling changes as well as conserved and context-specific signaling between uninfected SI sample and multiple samples with different *S.T* infection time points. We followed the typical procedure of the CellChat tutorial, which included several key steps: (1) data input, processing and initialization of CellChat object; (2) inference of cell-cell communication network; (3) comparison analysis of multiple datasets; (4) visualization of cell-cell communication network. Specifically, we began by preparing the normalized total RNA expression matrices as input data for CellChat. The processed data were used to initialize CellChat objects. Then we used the computeCommunProb function to generate the presumed ligand–receptor interaction pairs with "CellChatDB.mouse" data. To delve deeper into specific cell-cell interactions, particularly between 'late E' and 'CD8^{+} T' cell types on the MHC-I pathway, we applied the computeCommunProbPathway function. Last, the results were visualized with the functions in the CellChat full tutorial for comparison analysis of multiple datasets. (https://htmlpreview.github.io/?https://github.com/sqjin/CellChat/blob/master/tutorial/Comparison_analysis_of_multiple_datasets.html).

Data visualization
Plots were generated using the ggplot2 (version 3.4.2), cowplot (version 1.1.1), ggridges (version 0.5.4), ggrepel (version 0.9.1), ggpubr (version 0.4.0), circlize (0.4.15), ComplexHeatmap (version 2.11.1) and pheatmap (version 1.0.12) packages in R (version 4.0.4).

Real-time PCR (qRT-PCR)
Total RNA was extracted from corresponding samples with RNAprep Pure Micro Kit or TRIzol according to the manufacturer's protocol. Then cDNA was synthesized with the M-MLV reverse transcriptase (Promega, Madison, USA). mRNA transcripts were analyzed with ABI 7300 qPCR system using indicated primer pairs. The experiment was performed three times independently and the results were analyzed by $2^{-\Delta\Delta Ct}$ method. *Actb* or 18 s were used as endogenous control. Primers used in this study are listed in Supplementary Data 5.

Statistical analysis
Number of mice and experiments, and statistical tests are reported in each figure legend. For statistical analysis, data were analyzed with GraphPad Prism v10. Results are shown as means ± SEM. To compare differences between two groups, two-tailed unpaired Student's t-test was used. Differences among multiple groups were assessed using ANOVA with Tukey's multiple comparison test. The *p* values were provided in the figures.

Reporting summary
Further information on research design is available in the Nature Portfolio Reporting Summary linked to this article.

Data availability
Raw data and count matrices associated with this study have been deposited in the Gene Expression Omnibus (GEO) database under accession code GSE279651 (bone marrow data) (https://www.ncbi.nlm.nih.gov/geo/query/acc.cgi?acc=GSE279651) and GSE280764 (small intestine data) (https://www.ncbi.nlm.nih.gov/geo/query/acc.cgi?acc=GSE280764). The data used in the figures in this study are provided in the Source Data file. Source data are provided with this paper.

Code availability
Custom code is available freely from Github (https://github.com/wury24/scnewRNA-seq), (https://github.com/singleron-RD/CeleScope/blob/master/doc/assay/multi_dynaseq.md), and Zenodo (https://doi.org/10.5281/zenodo.15878358).

References
1. Wissink, E. M., Vihervaara, A., Tippens, N. D. & Lis, J. T. Nascent RNA analyses: tracking transcription and its regulation. *Nat. Rev. Genet.* **20**, 705–723 (2019).
2. Battich, N. et al. Sequencing metabolically labeled transcripts in single cells reveals mRNA turnover strategies. *Science* **367**, 1151–1156 (2020).
3. Erhard, F. et al. scSLAM-seq reveals core features of transcription dynamics in single cells. *Nature* **571**, 419–423 (2019).
4. Rabani, M. et al. High-resolution sequencing and modeling identifies distinct dynamic RNA regulatory strategies. *Cell* **159**, 1698–1710 (2014).
5. Ding, J., Sharon, N. & Bar-Joseph, Z. Temporal modelling using single-cell transcriptomics. *Nat. Rev. Genet.* **23**, 355–368 (2022).
6. Papalexi, E. & Satija, R. Single-cell RNA sequencing to explore immune cell heterogeneity. *Nat. Rev. Immunol.* **18**, 35–45 (2018).
7. Qiu, Q. et al. Massively parallel and time-resolved RNA sequencing in single cells with scNT-seq. *Nat. Methods* **17**, 991–1001 (2020).
8. Wan, Y. et al. Dynamic imaging of nascent RNA reveals general principles of transcription dynamics and stochastic splice site selection. *Cell* **184**, 2878–2895.e2820 (2021).
9. Drexler, H. L. et al. Revealing nascent RNA processing dynamics with nano-COP. *Nat. Protoc.* **16**, 1343–1375 (2021).
10. Matsushima, W. et al. Sequencing cell-type-specific transcriptomes with SLAM-ITseq. *Nat. Protoc.* **14**, 2261–2278 (2019).
11. Herzog, V. A. et al. Thiol-linked alkylation of RNA to assess expression dynamics. *Nat. Methods* **14**, 1198–1204 (2017).
12. Cao, J., Zhou, W., Steemers, F., Trapnell, C. & Shendure, J. Sci-fate characterizes the dynamics of gene expression in single cells. *Nat. Biotechnol.* **38**, 980–988 (2020).
13. Hendriks, G. J. et al. NASC-seq monitors RNA synthesis in single cells. *Nat. Commun.* **10**, 3138 (2019).
14. Paludan, S. R., Pradeu, T., Masters, S. L. & Mogensen, T. H. Constitutive immune mechanisms: mediators of host defence and immune regulation. *Nat. Rev. Immunol.* **21**, 137–150 (2021).
15. Greten, F. R. & Grivennikov, S. I. Inflammation and cancer: triggers, mechanisms, and consequences. *Immunity* **51**, 27–41 (2019).
16. Newton, K., Dixit, V. M. & Kayagaki, N. Dying cells fan the flames of inflammation. *Science* **374**, 1076–1080 (2021).
17. Stephenson, E. et al. Single-cell multi-omics analysis of the immune response in COVID-19. *Nat. Med.* **27**, 904–916 (2021).
18. Kotliar, D. et al. Single-cell profiling of Ebola virus disease in vivo reveals viral and host dynamics. *Cell* **183**, 1383–1401.e1319 (2020).
19. Besser, J. M. Salmonella epidemiology: a whirlwind of change. *Food Microbiol* **71**, 55–59 (2018).
20. Galán, J. E. Salmonella Typhimurium and inflammation: a pathogen-centric affair. *Nat. Rev. Microbiol.* **19**, 716–725 (2021).
21. Watcham, S., Kucinski, I. & Gottgens, B. New insights into hematopoietic differentiation landscapes from single-cell RNA sequencing. *Blood* **133**, 1415–1426 (2019).

22. Atlasi, Y. & Stunnenberg, H. G. The interplay of epigenetic marks during stem cell differentiation and development. *Nat. Rev. Genet.* **18**, 643–658 (2017).

23. Guilliams, M., Mildner, A. & Yona, S. Developmental and functional heterogeneity of monocytes. *Immunity* **49**, 595–613 (2018).

24. Ren, X. et al. COVID-19 immune features revealed by a large-scale single-cell transcriptome atlas. *Cell* **184**, 1895–1913.e1819 (2021).

25. Saliba, A. E. et al. Single-cell RNA-seq ties macrophage polarization to growth rate of intracellular Salmonella. *Nat. Microbiol.* **2**, 16206 (2016).

26. Shalek, A. K. et al. Single-cell RNA-seq reveals dynamic paracrine control of cellular variation. *Nature* **510**, 363–369 (2014).

27. La Manno, G. et al. RNA velocity of single cells. *Nature* **560**, 494–498 (2018).

28. Qiu, X. et al. Mapping transcriptomic vector fields of single cells. *Cell* **185**, 690–711.e645 (2022).

29. Rabani, M. et al. Metabolic labeling of RNA uncovers principles of RNA production and degradation dynamics in mammalian cells. *Nat. Biotechnol.* **29**, 436–442 (2011).

30. Schwalb, B. et al. TT-seq maps the human transient transcriptome. *Science* **352**, 1225–1228 (2016).

31. Ng, L. G., Ostuni, R. & Hidalgo, A. Heterogeneity of neutrophils. *Nat. Rev. Immunol.* **19**, 255–265 (2019).

32. Evrard, M. et al. Developmental analysis of bone marrow neutrophils reveals populations specialized in expansion, trafficking, and effector functions. *Immunity* **48**, 364–379.e368 (2018).

33. Xie, X. et al. Single-cell transcriptome profiling reveals neutrophil heterogeneity in homeostasis and infection. *Nat. Immunol.* **21**, 1119–1133 (2020).

34. Shvedunova, M. & Akhtar, A. Modulation of cellular processes by histone and non-histone protein acetylation. *Nat. Rev. Mol. Cell Biol.* **23**, 329–349 (2022).

35. Meyer, K. D. & Jaffrey, S. R. The dynamic epitranscriptome: N6-methyladenosine and gene expression control. *Nat. Rev. Mol. Cell Biol.* **15**, 313–326 (2014).

36. Kayama, H., Okumura, R. & Takeda, K. Interaction between the microbiota, epithelia, and immune cells in the intestine. *Annu. Rev. Immunol.* **38**, 23–48 (2020).

37. Voskoboinik, I., Whisstock, J. C. & Trapani, J. A. Perforin and granzymes: function, dysfunction and human pathology. *Nat. Rev. Immunol.* **15**, 388–400 (2015).

38. Walch, M. et al. Cytotoxic cells kill intracellular bacteria through granulysin-mediated delivery of granzymes. *Cell* **161**, 1229 (2015).

39. Bunker, J. J. & Bendelac, A. IgA responses to microbiota. *Immunity* **49**, 211–224 (2018).

40. Chen, K., Magri, G., Grasset, E. K. & Cerutti, A. Rethinking mucosal antibody responses: IgM, IgG and IgD join IgA. *Nat. Rev. Immunol.* **20**, 427–441 (2020).

41. Bunker, J. J. et al. Natural polyreactive IgA antibodies coat the intestinal microbiota. *Science* **358**, eaan6619 (2017).

42. Pabst, O. & Slack, E. IgA and the intestinal microbiota: the importance of being specific. *Mucosal Immunol.* **13**, 12–21 (2020).

43. Kirkland, D. et al. B cell-intrinsic MyD88 signaling prevents the lethal dissemination of commensal bacteria during colonic damage. *Immunity* **36**, 228–238 (2012).

44. Moor, A. E. et al. Spatial reconstruction of single enterocytes uncovers broad zonation along the intestinal villus axis. *Cell* **175**, 1156–1167.e1115 (2018).

45. Yu, S. et al. Paneth cell-derived lysozyme defines the composition of mucolytic microbiota and the inflammatory tone of the intestine. *Immunity* **53**, 398–416.e398 (2020).

46. Xie, Z. et al. The gut-to-brain axis for toxin-induced defensive responses. *Cell* **185**, 4298–4316.e4221 (2022).

47. Malik, A. et al. Epithelial IFNγ signalling and compartmentalized antigen presentation orchestrate gut immunity. *Nature* **623**, 1044–1052 (2023).

48. Schlesinger, S. & Meshorer, E. Open chromatin, epigenetic plasticity, and nuclear organization in pluripotency. *Dev. Cell* **48**, 135–150 (2019).

49. Zheng, H. & Xie, W. The role of 3D genome organization in development and cell differentiation. *Nat. Rev. Mol. Cell Biol.* **20**, 535–550 (2019).

50. Heyman, O. et al. Paired single-cell host profiling with multiplex-tagged bacterial mutants reveals intracellular virulence-immune networks. *Proc. Natl. Acad. Sci. USA* **120**, e2218812120 (2023).

51. Dotiwala, F. et al. Killer lymphocytes use granulysin, perforin and granzymes to kill intracellular parasites. *Nat. Med.* **22**, 210–216 (2016).

52. Kiniry, B. E. et al. Predominance of weakly cytotoxic, T-bet(Low) Eomes(Neg)CD8(+) T-cells in human gastrointestinal mucosa: implications for HIV infection. *Mucosal Immunol.* **10**, 1008–1020 (2017).

53. Biton, M. et al. T helper cell cytokines modulate intestinal stem cell renewal and differentiation. *Cell* **175**, 1307–1320.e1322 (2018).

54. He, K. et al. Gasdermin D licenses MHCII induction to maintain food tolerance in small intestine. *Cell* **186**, 3033–3048.e3020 (2023).

55. Koyama, M. et al. MHC class II antigen presentation by the intestinal epithelium initiates graft-versus-host disease and is influenced by the microbiota. *Immunity* **51**, 885–898.e887 (2019).

56. Xiong, Z. et al. Intestinal Tuft-2 cells exert antimicrobial immunity via sensing bacterial metabolite N-undecanoylglycine. *Immunity* **55**, 686–700.e687 (2022).

57. Jürges, C., Dölken, L. & Erhard, F. Dissecting newly transcribed and old RNA using GRAND-SLAM. *Bioinformatics* **34**, i218–i226 (2018).

58. Korsunsky, I. et al. Fast, sensitive and accurate integration of single-cell data with Harmony. *Nat. Methods* **16**, 1289–1296 (2019).

59. Jin, S. et al. Inference and analysis of cell-cell communication using CellChat. *Nat. Commun.* **12**, 1088 (2021).

Acknowledgements

Author contributions

Z.X. designed and performed experiments, analyzed data and wrote the paper. R.Y.W. and Y.X.W. generated scIVNL-seq method and analyzed the data. Y.W.X., C.Z.L., D.Y.K. and Z.Q.X. performed some of the experiments and analyzed some of the data. P.K.Z., Z.L.W., P.Z., Y.D., H.G. and P.P.Z. provided technical assistance. S.M.H. performed data processing and analyzed data, and Z.S.F. initiated the study, organized, designed, and wrote the paper.

Competing interests

The authors declare no competing interests.

Additional information

Supplementary information The online version contains supplementary material available at https://doi.org/10.1038/s41467-025-63155-1.

Correspondence and requests for materials should be addressed to Shunmin He or Zusen Fan.

Peer review information *Nature Communications* thanks the anonymous reviewers for their contribution to the peer review of this work. A peer review file is available.

Reprints and permissions information is available at http://www.nature.com/reprints

Publisher's note Springer Nature remains neutral with regard to jurisdictional claims in published maps and institutional affiliations.